PHYSICAL REVIEW B **109**, 195405 (2024)

Microscopic Green's function approach for generalized Dirac Hamiltonians

Jeyson Támara-Isaza,[1,2] Pablo Burset,[3] and William J. Herrera[1]
[1] *Departamento de Física, Universidad Nacional de Colombia, 110911 Bogotá, Colombia*
[2] *Quantum Technology Center, University of Maryland, College Park, Maryland, 20742, USA*
[3] *Department of Theoretical Condensed Matter Physics, Condensed Matter Physics Center (IFIMAC) and Instituto Nicolás Cabrera, Universidad Autónoma de Madrid, 28049 Madrid, Spain*

(Received 7 September 2023; revised 20 December 2023; accepted 21 March 2024; published 2 May 2024)

The rising interest in Dirac materials, condensed-matter systems where low-energy electronic excitations are described by the relativistic Dirac Hamiltonian, entails a need for microscopic effective models to analytically describe their transport properties. Specifically, for the study of quantum transport these effective models must take into account the effect of microscopic scale interfaces and the presence of well-defined edges, while reproducing the correct band structure. We develop a general method to analytically compute the microscopic Green's function of Dirac materials valid for infinite, semi-infinite, and finite two-dimensional layers with zigzag or armchair edge orientations. We test our method computing the density of states, scattering probabilities and topological properties of germanene and semiconducting transition metal dichalcogenides, obtaining simple analytical formulas. Our results provide a useful analytical tool with low computational cost for the interpretation of transport experiments on Dirac materials which could be extended to describe additional degrees of freedom like extra layers, superconductivity, etc.

DOI: 10.1103/PhysRevB.109.195405

I. INTRODUCTION

Two-dimensional (2D) materials have become an excellent playground to engineer quantum devices with exotic properties [1–6]. Examples include one- or few-atom-thick materials like graphene, silicene, stanene, germanene, and transition-metal dichalcogenides (TMDs) [7–10]. Despite their differences, many of these materials share low-energy characteristics like the presence of nodal points or a linear band dispersion, tunable carrier density, and high mobility due to suppressed backscattering [11–13]. All these properties make them very promising candidates for quantum transport applications [5,14–18]. This class of condensed-matter systems is known as Dirac materials since, in the infrared regime, charge carriers follow a relativistic Dirac equation yielding the same universal behavior for, e.g., the optical conductivity or the specific heat [12,13,19,20]. The origin of the Dirac-like behavior varies with the material but in all cases some specific symmetries protect the formation of Dirac nodes in the spectrum [19]. For example, in the recently discovered quantum spin Hall insulator [21,22] time-reversal symmetry promotes and protects the formation of Dirac-like metallic one-dimensional (1D) edge states on an otherwise 2D insulator. Similarly, three-dimensional (3D) topological insulators feature 2D edge states described by a single (or an odd number of) Dirac cones [23–27].

Dirac materials are characterized by their band structure [7–10], and new materials can be predicted from numerical methods [28], like density functional theory or *ab initio* calculations [29]. Once identified, their microscopic properties are more easily accessed by numerical lattice calculations [30–36], which can include finite-size effects and the presence of edges [37,38]. For the study of quantum transport, it is also important to include the effect of atomic scale interfaces, or the presence of well-defined edges in layers of 2D materials; for example, the electronic spectrum of a graphene nanoribbon strongly depends on the edge orientation [39–41].

In a complementary approach, low-energy, effective microscopic Hamiltonians offer a way to include all these effects (finite-size, edges and interfaces, etc.), while, at the same time, providing analytical results for the study of transport [39]. In the absence of Coulomb interactions, a scattering theory can be derived from the Dirac Hamiltonian including interesting effects like edge orientation, spin-orbit coupling, magnetization, or even superconductivity [42–52]. A particularly interesting generalization of effective Hamiltonians are the Green's function (GF) methods combined with Dyson's equation [40,43]. The GF facilitates the study of correlations (interactions, superconductivity, etc.) while naturally allowing the computation of observables like the electric current and the density of states. The Hamiltonian approach to GF techniques is perfectly suited to consider edge and interface effects in 2D systems and, in many cases, provides simple, analytical results which can also describe long-range order like magnetism or superconductivity [43,49,53,54].

In this work, we develop a systematic and general method to analytically compute the microscopic GF of systems with a general Dirac Hamiltonian and apply this method to 2D honeycomb structure. The resulting GF accounts for the presence of well-defined edges or interfaces at the atomic scale. We then obtain the GF of relevant Dirac materials, like germanene and TMDs, and obtain transport properties (density of states and scattering probabilities) of infinite, semi-infinite, and finite layers. Our general method can distinguish specific edge orientations like zigzag, which only involves one Dirac node or valley, and armchair that combines two valleys. In all cases, our method provides simple analytical formulas, with low computational cost, which allow us to compute the formation of edge states and their topological properties.

The rest of the paper is organized as follows: In Sec. II, we present the general Dirac Hamiltonian and calculate the related GF. Then, in Secs. III and IV, we develop the recipe for the GF of a semi-infinite and a finite system, respectively. In Secs. V and VI, we apply our method to zigzag and armchair edge orientations and include specific applications for TMDs and germanene. We then explore the interesting behavior of germanene under an out-of-plane electric field in Sec. VII. Finally, we present some concluding remarks in Sec. VIII. An Appendix has also been added to show details of the calculations.

II. GENERALIZED DIRAC HAMILTONIAN

We consider the following general Dirac Hamiltonian, acting on a two-dimensional space

$$\check{H}(x,y) = -i\hbar v_F(\check{\alpha}_x\partial_x + \check{\alpha}_y\partial_y) + \check{V}(x,y), \tag{1}$$

with v_F the Fermi velocity and $\check{V}(x,y)$ an electrostatic potential. Here, $\check{\alpha}_{x,y}$ are $2N \times 2N$ matrices acting on the SU(2) degree of freedom that defines the Dirac Hamiltonian and the N-dimensional space containing the rest of degrees of freedom. In the following, we assume translation invariance along the y axis, with $k_y \equiv q$ a conserved quantity, and consider inhomogeneous systems along the x direction. Then, Eq. (1) reduces to $\check{H}_q = -i\hbar\partial_x\check{\alpha}_x + q\check{\alpha}_y + \check{V}(x)$, which obeys the generalized Dirac equation

$$\check{H}_q\psi_q(x,y) = E_q\psi_q(x,y), \tag{2}$$

with solutions of the form

$$\psi_q(x,y) = \mathrm{e}^{iqy}[\psi_n^+\mathrm{e}^{ik_n^+x} + \psi_n^-\mathrm{e}^{ik_n^-x}], \tag{3}$$

where $\psi_n = (\psi_n^+, \psi_n^-)^T$ are $2N$-dimensional spinors in the SU(2) space spawned by $\check{\alpha}_x$, with n labeling the other quantum numbers. The states $\psi_n^\pm\mathrm{e}^{ik_n^\pm x}$, where, usually, $k_n^- = -k_n^+$, represent right-moving (ψ_n^+) and left-moving (ψ_n^-) solutions along the x direction with probability flux current given by $J_{n,x}^\pm = v_F\psi_n^{\pm\dagger}\check{\alpha}_x\psi_n^\pm = \pm v_F$. These states are not, however, orthogonal. To obtain an orthogonality relation, we must define the states

$$\tilde{\psi}_n^\pm = \pm\check{\alpha}_x^\dagger\psi_n^\pm, \quad (\tilde{\psi}_n^\pm)^\dagger = \pm(\psi_n^\pm)^\dagger\check{\alpha}_x, \tag{4}$$

which fulfill

$$\left(\tilde{\psi}_n^\varepsilon\right)^\dagger\psi_m^{\varepsilon'} = \delta_{nm}\delta_{\varepsilon\varepsilon'}, \tag{5}$$

with $\varepsilon = +, -$. Combining $\psi_n^\pm$ and $\tilde{\psi}_n^\pm$ states we then find the completeness relation

$$\sum_{\varepsilon,n}\psi_n^\varepsilon\left(\tilde{\psi}_n^\varepsilon\right)^\dagger = \check{1}, \tag{6}$$

with $\check{1}$ being the $2N \times 2N$ unit matrix.

We can now define the general GF associated with the Dirac Hamiltonian in Eq. (2) as

$$(E\check{1} - \check{H}_q)\check{G}_q(x,x') = E\delta(x-x')\check{1}. \tag{7}$$

The subindex in $\check{G}_q(x,x')$ indicates the quasi-one-dimensional regime where q is a conserved quantity. We henceforth work in this regime and omit the subindex. Assuming $\check{V}(x) = 0$ and $k_n^- = -k_n^+ = -k_n$, with $k_n \geqslant 0$, the GF $\check{g}(x,x')$ of the unbounded (bulk) system becomes [43]

$$\check{g}^<(x<x',x') = \frac{-i}{2\hbar v_F}\sum_n f_n^-(x-x')\psi_n^-(\bar{\psi}_n^-)^T, \tag{8a}$$

$$\check{g}^>(x>x',x') = \frac{-i}{2\hbar v_F}\sum_n f_n^+(x-x')\psi_n^+(\bar{\psi}_n^+)^T. \tag{8b}$$

The superindex $\check{g}^{\gtrless} = \check{g}(x \gtrless x')$ indicates the different form of the GF depending on the spatial coordinates. When it is important to distinguish the cases with $x \gtrless x'$ we show this superindex and omit it otherwise. The x dependence is encoded in the functions $f_n^\varepsilon(x) = \mathrm{e}^{i\varepsilon k_n x}$, and the states $\bar{\psi}_n^\varepsilon$ are solutions to the transposed Hamiltonian in Eq. (1). Transposing a Dirac Hamiltonian results in the exchange $\mathbf{k} \to -\mathbf{k}$, so the transposed states can be related to the left- and right-moving states in Eq. (3) as

$$\bar{\psi}_n^{+T} = (\check{\gamma}\psi_n^-)^T, \quad \bar{\psi}_n^{-T} = (\check{\gamma}\psi_n^+)^T, \tag{9}$$

with $\check{\gamma}$ a matrix such that the scalar product $\psi^\dagger\check{\gamma}\psi$ is invariant under Lorentz transformations and spatial inversion [43].

III. SEMI-INFINITE SYSTEMS

We can define a sharp edge localized at $x = x_a$ by means of the perturbation potential

$$\check{V}(x) = U_a\check{\tau}_a\delta(x_a - x), \tag{10}$$

with U_a the potential strength that takes the limit $U_a \to \infty$ when we consider the edge of a semi-infinite layer. Here, $\check{\tau}_a$ is a matrix that encodes the specific boundary conditions at the edge and takes into account the change in sublattice associated with atomic-scale translations [43]. The GF perturbed by this potential is given by Dyson's equation as

$$\begin{aligned}\check{G}_a(x,x') &= \check{g}(x,x') + \int \mathrm{d}x_1\check{g}(x,x_1)\check{V}(x_1)\check{G}_a(x_1,x') \\ &= \check{g}(x,x') + \check{g}(x,x_a)U_a\check{\tau}_a\check{G}_a(x_a,x'),\end{aligned} \tag{11}$$

with $\check{g}(x,x')$ the bulk GF defined in Eq. (8). The perturbation potential Eq. (10) can also be used to join two semi-infinite solutions, Eq. (11), and recover the bulk result [43]. The solution of this equation when both x and x' are on the right (left) of x_a takes the form

$$\check{G}_a^{R(L)}(x,x') = \check{g}(x,x') + \check{Q}^{>(<)}(x)\check{g}^{<(>)}(x_a,x'), \tag{12}$$

with the superindex R (L) indicating that $x, x' > x_a$ ($x, x' < x_a$), and where we have defined

$$\check{Q}^\chi(x) = \check{g}^\chi(x,x_a)U_a\check{\tau}_aD^\chi, \tag{13}$$

$$\check{D}_a^\chi = (\check{1} - \check{g}^\chi(x_a,x_a)U_a\check{\tau}_a)^{-1}, \tag{14}$$

with $\chi =>, <$. An iterative method allows us to find an expression for Eq. (13) as (see Sec. A for details)

$$\check{Q}^\chi(x) = U_a\check{g}^\chi(x,x_a)\check{\tau}_a\sum_{p=0}^{\infty}[U_a\check{g}^\chi(x_a,x_a)\check{\tau}_a]^p. \tag{15}$$

Using the completeness relation, Eq. (6), we find

$$\begin{aligned}\check{g}^{>}(x_a, x_a)\check{\tau}_a &= \frac{-i}{2\hbar v_F}\sum_n \psi_n^{+}(\bar{\psi}_n^{+})^T\check{\tau}_a\sum_{m,\varepsilon}\psi_m^{\varepsilon}\big(\tilde{\psi}_m^{\varepsilon}\big)^{\dagger}\\ &= \frac{-i}{2\hbar v_F}\sum_{n,m,\varepsilon}\tau_{a,nm}^{+\varepsilon}\check{P}_{nm}^{+\varepsilon}, \end{aligned} \tag{16}$$

where we have defined the projector operators

$$\check{P}_{nm}^{\varepsilon\varepsilon'} = \psi_n^{\varepsilon}\big(\tilde{\psi}_m^{\varepsilon'}\big)^{\dagger}, \tag{17}$$

and the matrix representation of $\check{\tau}_a$ as

$$\tau_{a,nm}^{\varepsilon\varepsilon'} = \big(\bar{\psi}_n^{\varepsilon}\big)^T\check{\tau}_a\psi_m^{\varepsilon'}. \tag{18}$$

In what follows, it is more insightful to write explicitly the subspace spawned by the left- and right-moving solutions of Eq. (2), that is, the $N\times N$ matrices $\hat{\tau}^{\varepsilon\varepsilon'}$, so that

$$\check{\tau} = \begin{pmatrix}\hat{\tau}^{++} & \hat{\tau}^{+-}\\ \hat{\tau}^{-+} & \hat{\tau}^{--}\end{pmatrix}. \tag{19}$$

We thus use the symbols $\check{\ldots}$ and $\hat{\ldots}$ to distinguish the full $2N\times 2N$ matrices from others with reduced $N\times N$ dimensions. As a result, Eq. (13) becomes

$$\check{Q}^{>}(x) = \sum_{n,m,\varepsilon} f_n^{+}(x-x_a)\big(\hat{r}_a^{+\varepsilon}\big)_{nm}\check{P}_{nm}^{+\varepsilon}, \tag{20}$$

with $\hat{r}_a^{+\varepsilon} = \hat{D}_a^{+}\hat{\tau}_a^{+\varepsilon}$ and

$$\hat{D}_a^{\varepsilon} = \frac{-iU_a}{2\hbar v_F}\left(1 + \frac{iU_a}{2\hbar v_F}\hat{\tau}_a^{\varepsilon\varepsilon}\right)^{-1}. \tag{21}$$

Analogously,

$$\check{Q}^{<}(x) = \sum_{n,m,\varepsilon} f_n^{-}(x-x_a)\big(\hat{r}_a^{-\varepsilon}\big)_{nm}\check{P}_{nm}^{-\varepsilon}, \tag{22}$$

with $\hat{r}_a^{-\varepsilon} = \hat{D}_a^{-}\hat{\tau}_a^{-\varepsilon}$.

Consequently, the local GFs at each side of the perturbation adopt the form

$$\begin{aligned}&\check{G}_a^{R}(x, x')\\ &\quad = \check{g}(x, x') + \sum_{nm} f_n^{+}(x-x_a)(\hat{r}_a^{+-})_{nm}f_m^{-}(x_a - x')\psi_n^{+}(\bar{\psi}_m^{-})^T,\end{aligned} \tag{23}$$

and

$$\begin{aligned}&\check{G}_a^{L}(x, x')\\ &\quad = \check{g}(x, x') + \sum_{nm} f_n^{-}(x-x_a)(\hat{r}_a^{-+})_{nm}f_m^{+}(x_a - x')\psi_n^{-}(\bar{\psi}_m^{+})^T.\end{aligned} \tag{24}$$

Here, $\check{r}_a$ corresponds to the scattering matrix of reflection amplitudes. For a potential acting on x_a, we can define the transmission amplitudes as $\hat{t}_a^{\varepsilon\varepsilon} = \hat{1} + \hat{r}_a^{\varepsilon\varepsilon}$, and the scattering matrix results in

$$\check{S}_a = \check{1} + \check{r}_a = \begin{pmatrix}\hat{t}_a^{++} & \hat{r}_a^{+-}\\ \hat{r}_a^{-+} & \hat{t}_a^{--}\end{pmatrix}, \tag{25}$$

which fulfills the unitarity condition $\check{S}_a\check{S}_a^{\dagger} = \check{S}_a^{\dagger}\check{S}_a = \check{1}$; for more details we refer the reader to Sec. B.

The semi-infinite system requires a hard edge at $x = x_a$, which we obtain taking the limit $U_a \to \infty$. Consequently, the denominators in Eq. (21) become $\hat{D}_a^{\varepsilon} \to -(\hat{\tau}_a^{\varepsilon\varepsilon})^{-1}$. The scattering matrix for the semi-infinite system thus reduces to

$$\check{S}_a = \begin{pmatrix} 0 & (\hat{\tau}_a^{++})^{-1}\hat{\tau}_a^{+-}\\ (\hat{\tau}_a^{--})^{-1}\hat{\tau}_a^{-+} & 0\end{pmatrix}, \tag{26}$$

where the transmission amplitudes are zero at the edge. As a result, the matrix of reflection amplitudes is unitary, $(\hat{r}_a^{+-})^{\dagger} = (\hat{r}_a^{+-})^{-1}$, and, therefore, $[(\hat{\tau}_a^{++})^{-1}]^{\dagger}(\hat{\tau}_a^{+-})^{\dagger} = (\hat{\tau}_a^{+-})^{-1}\hat{\tau}_a^{++}$.

IV. NANORIBBON

We now extend the previous results to include a second edge potential barrier as $\check{V}(x) = \sum_{j=a}^{b} U_j\check{\tau}_j\delta(x_j - x)$. We approach this problem sequentially by first considering only one edge potential. For example, by taking $U_b = 0$, we find, from Eq. (11),

$$\check{G}_a(x, x') = \check{g}(x, x') + \check{g}(x, x_a)U_a\check{\tau}_a\check{G}_a(x_a, x'). \tag{27}$$

Similarly, by taking $U_a = 0$ and $U_b \neq 0$, we obtain $\check{G}_b(x, x')$. Restricting ourselves to the region where $x_a \leqslant x, x' \leqslant x_b$, the GF $\check{G}_a(x, x')$ becomes of *right* type, Eq. (23), for barrier potential $U_a\check{\tau}_a$, while $\check{G}_b(x, x')$ for barrier potential $U_b\check{\tau}_b$ is of *left* type, Eq. (24). For simplicity, we thus omit the superindexes R and L. We apply again Dyson's equation to Eq. (27) to introduce the edge potential U_b and reach

$$\begin{aligned}\check{G}_{ab}(x, x') &= \check{G}_a(x, x') + \check{G}_a^{<}(x, x_b)U_b\check{\tau}_b\\ &\quad\times(1 - \check{G}_a^{<}(x_b, x_b)U_b\check{\tau}_b)^{-1}\check{G}_a^{>}(x_b, x'),\end{aligned} \tag{28}$$

with $\check{G}^{\gtrless} = \check{G}(x \gtrless x')$, cf. Eq. (8). The solution to Eq. (28) reads

$$\check{G}_{ab}(x, x') = \check{G}_a(x, x') + \check{Q}^{<}(x)\check{G}_a^{>}(x_b, x'), \tag{29}$$

with

$$\check{Q}^{<}(x) = \sum_{n,m,\varepsilon,\varepsilon'} f_n^{\varepsilon}(x - x_b)\big(\hat{r}_b^{\varepsilon\varepsilon'}\big)_{nm}\check{P}_{nm}^{\varepsilon\varepsilon'}, \tag{30}$$

and

$$\check{r}_b = -i\frac{U_b\check{\tau}_b}{2\hbar v_F}\left(\check{1} + i\frac{U_b\check{\tau}_b}{2\hbar v_F}\right)^{-1}. \tag{31}$$

Using the explicit expression for the semi-infinite GF, Eq. (23), we write the GF with $x > x'$ for the central region as

$$\begin{aligned}&\check{G}_{ab}^{>}(x, x')\\ &\quad = \frac{-i}{2\hbar v_F}\sum_{n,m,\varepsilon,\varepsilon'} f_n^{\varepsilon}(x - x_b)(\check{w}^{>})_{nm}^{\varepsilon\varepsilon'}f_m^{\varepsilon'}(x_b - x')\psi_n^{\varepsilon}\big(\bar{\psi}_m^{\varepsilon'}\big)^T,\end{aligned} \tag{32}$$

where we have defined the matrices

$$\check{w}^{>} = \begin{pmatrix}\hat{1} + \hat{w}_b^{++} & (\hat{1} + \hat{w}_b^{++})\hat{r}_a^{+-}(W)\\ \hat{w}_b^{-+} & \hat{w}_b^{-+}\hat{r}_a^{+-}(W)\end{pmatrix}, \tag{33}$$

with $W = x_b - x_a > 0$ the width of the finite region. Here, $\hat{w}_b^{\varepsilon\varepsilon'}$ are the submatrix elements of

$$\check{w}_b = -i\frac{U_b}{2\hbar v_F}\check{\tau}\left(\check{1} + i\frac{U_b}{2\hbar v_F}\check{\tau}\right)^{-1}, \tag{34}$$

with

$$\check{\tau} = \begin{pmatrix} \hat{r}_a^{+-}(W)\hat{\tau}_b^{-+} & \hat{r}_a^{+-}(W)\hat{\tau}_b^{--} \\ \hat{\tau}_b^{-+} & \hat{\tau}_b^{--} \end{pmatrix}, \tag{35}$$

and $\hat{r}_a^{+-}(W)$ is defined from the reflection matrix at the left interface, $\hat{r}_a^{+-}$, as $\hat{r}_a^{+-}(W) = \hat{f}^{++}(-W)\hat{r}_a^{+-}\hat{f}^{--}(W)$, with the diagonal matrices $(\hat{f}^{\varepsilon\varepsilon})_{nm}(x) = \delta_{nm}f_m^{\varepsilon}(x)$. Analogously, we can also define

$$\check{w}^{<} = \begin{pmatrix} \hat{w}_b^{++} & (\hat{1} + \hat{w}_b^{++})\hat{r}_a^{+-}(W) \\ \hat{w}_b^{-+} & \hat{1} + \hat{w}_b^{-+}\hat{r}_a^{+-}(W) \end{pmatrix}, \tag{36}$$

where we have used the projector operators, Eq. (17). This result is equivalent to the reflection matrix for a single barrier at $x = x_b$, $\hat{r}^{++}$, changing $\check{w}_b$ by $\hat{\tau}^{++}$.

To obtain the GF of a nanoribbon we must take the limits $U_{a,b} \to \infty$, obtaining

$$\check{G}_{ab}^{\lessgtr}(x, x') = \frac{-i}{2\hbar v_F}\sum_{\substack{n,m \\ \varepsilon,\varepsilon'}} f_n^{\varepsilon}(x)(\check{w}^{\lessgtr})_{nm}^{\varepsilon\varepsilon'}f_m^{\varepsilon'}(-x')\psi_n^{\varepsilon}(\bar{\psi}_m^{\varepsilon'})^T, \tag{37}$$

where Eqs. (33) and (36) reduce to

$$\check{w}^{>} = \begin{pmatrix} \hat{D}^{++} & \hat{D}^{++}\hat{r}_a^{+-}(x_a) \\ \hat{r}_b^{-+}(x_b)\hat{D}^{++} & \hat{r}_b^{-+}(x_b)\hat{D}^{++}\hat{r}_a^{+-}(x_a) \end{pmatrix}, \tag{38a}$$

$$\check{w}^{<} = \begin{pmatrix} \hat{D}^{++}\hat{r}_a^{+-}(x_a)\hat{r}_b^{-+}(x_b) & \hat{D}^{++}\hat{r}_a^{+-}(x_a) \\ \hat{r}_b^{-+}(x_b)\hat{D}^{++} & \hat{D}^{--} \end{pmatrix}, \tag{38b}$$

with

$$\hat{r}_a^{+-}(x_a) = \hat{f}^{++}(-x_a)\hat{r}_a^{+-}\hat{f}^{--}(x_a), \tag{39a}$$

$$\hat{r}_b^{-+}(x_b) = \hat{f}^{--}(x_b)\hat{r}_b^{-+}\hat{f}^{++}(-x_b), \tag{39b}$$

$$\hat{D}^{++} = [\hat{1} - \hat{r}_a^{+-}(x_a)\hat{r}_b^{-+}(x_b)]^{-1}, \tag{39c}$$

$$\hat{D}^{--} = [\hat{1} - \hat{r}_b^{-+}(x_b)\hat{r}_a^{+-}(x_a)]^{-1}. \tag{39d}$$

The latter equations allow us to obtain the bound states of the finite region by taking the condition $\hat{D}^{\pm\pm} = 0$, or, analogously, $\hat{r}_a^{+-}(x_a)\hat{r}_b^{-+}(x_b) = \hat{1}$. Consequently, the bound states of the finite region are tied to the reflection matrices at each independent edge.

V. DIRAC SYSTEM WITH ZIGZAG EDGES

Having established the general method for the computation of the GF of a Dirac system, we now present some examples showcasing specific edge orientations. We start with layers ending in zigzag edges, see Fig. 1, and modify the Hamiltonian of an infinite system, Eq. (1), so that it describes the low-energy physics of graphene-like materials like germanene, silicene, and TMDs. We thus get the Hamiltonian

$$\check{H}_{s\eta}(\mathbf{k}) = \mu_{s\eta}\check{\sigma}_0 + \hbar v_F(k\check{\sigma}_x + \eta q\check{\sigma}_y) + m_{s\eta}\check{\sigma}_z, \tag{40}$$

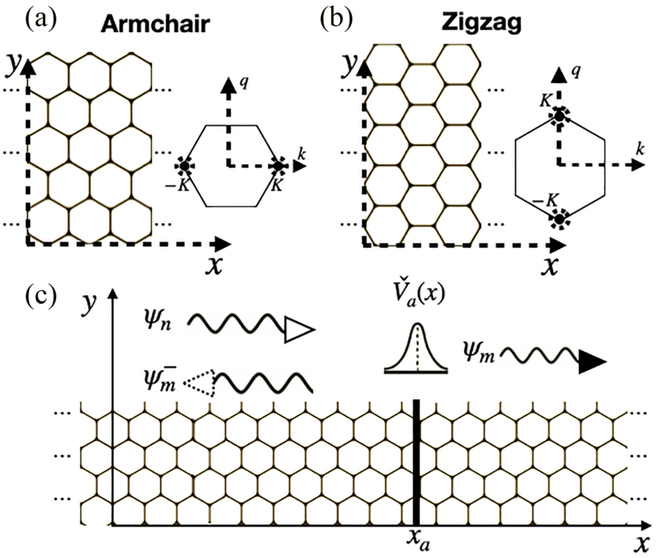

FIG. 1. Real-space atomic (a) armchair and (b) zigzag terminations, with their corresponding reciprocal unit cell showing K and $K' = -K$ valleys. (c) Perturbation potential forming two semi-infinite layers at $x = x_a$. The arrows correspond to the incident (ψ_n) and scattered wave functions (ψ_m and ψ_m^-).

with

$$\mu_{s\eta} = -E_F + \eta s\lambda_{SO}, \tag{41}$$

$$m_{s\eta} = \lambda_z - \eta s\lambda_{SO} + s\lambda_{AF} + \frac{\Delta}{2}. \tag{42}$$

Here, the Pauli matrices $\check{\sigma}_{0,x,y,z}$ act in sublattice space denoted by A- and B-type atoms, $\psi = (\psi_A, \psi_B)^T$, and the parameters $\eta = \pm$ and $s = \pm$ are the valley index and the spin S_z component, respectively. The Fermi velocity is written in terms of the lattice constant a and the hopping parameter t as $v_F = \sqrt{3}at/(2\hbar)$. Our approach assumes the $\mathbf{k}\cdot\mathbf{p}$ approximation where the relevant energy scales are comparable to t [35,39,55,56]. The 2×2 zigzag Hamiltonian in Eq. (40) thus corresponds to the case with $N = 1$, cf. Eqs. (2), (3), (19), so the symbols $.\hat{.}.$ denote here scalars. This Hamiltonian describes each of the inequivalent valleys K and K' separately, which for zigzag terminations are located at $\mathbf{k} = (k_x, k_y) \to (0, \pm K)$, see Fig. 1(b). The conserved momentum $\hbar q$ along the k_y direction is thus defined with respect to each valley [55] (e.g., $k_y \to K + q$ for valley K).

The parameter $m_{s\eta}$ describes a generic mass term given by the intrinsic gap Δ, and extra terms that depend on the specific material. For example, λ_{SO} represents the spin-orbit coupling, λ_{AF} a magnetic gap, and λ_z the energy due to an external electrical field perpendicular to the monolayer. Indeed, λ_{SO} is strong in systems such as germanene, silicene, and TMDs, but negligible in graphene. A magnetic material in close contact to the monolayer can induce a magnetization λ_{AF} by proximity effect. Previous works have analyzed the effect on the electronic state of the system caused by an electric field applied perpendicularly to monolayer of TMDs, germanene, or silicene [35,57,58]. Here, we represent this effect by the parameter λ_z which, being proportional to $\check{\sigma}_z$, breaks sublattice symmetry and is only possible in the presence of lattice buckling. Finally, the doping level $\mu_{s\eta}$ is determined by the Fermi energy E_F and, if present, the spin-orbit coupling λ_{SO}. In general, manipulating the Fermi energy E_F in isolated samples trivially shifts the spectrum without relevant consequences as we show in Sec. E. Consequently, we henceforth set $E_F = 0$.

The eigenstates of Eq. (40) can be found in Sec. D, with transposed states defined using Eq. (9) and $\check{\gamma} = \check{\sigma}_z$. With these states, the GF of the bulk system is given by Eq. (8). The resulting wave vectors are $k_{s\eta}^{\pm} = \pm k_{s\eta}$, where

$$k_{s\eta} = \sqrt{(E-\mu_{s\eta})^2 - m_{s\eta}^2 - (\hbar v_F q)^2}/(\hbar v_F). \tag{43}$$

For a given excitation energy E, the conserved momentum parallel to the interface $\hbar q$ can be parametrized by the angle $\alpha_{s\eta}$ defined as

$$e^{\pm i\alpha_{s\eta}} = \hbar v_F \frac{k_{s\eta} \pm iq}{\sqrt{(\mu_{s\eta}-E)^2 - m_{s\eta}^2}}. \tag{44}$$

We can now define the spectral density of states from the retarded GF as

$$\rho(E,q,x) = \frac{1}{\pi}\mathrm{Im}\{\mathrm{Tr}[\check{G}(E;q;x,x)]\}, \tag{45}$$

and the local density of states (LDOS) is then

$$\rho_T(E,x) = \int \rho(E;q;x)\mathrm{d}q. \tag{46}$$

The bulk spectral density for a given spin-valley configuration adopts the simple form $\rho_{T,s\eta} = 1/(\pi\hbar v_F k_{s\eta})$. Henceforth, we normalize the spectral density of states by $\rho_0 = ta$, which is equivalent to measuring energies and distances in units of the hopping t and the lattice constant a, respectively. We now proceed to define and apply the edge potentials to obtain the GF of a semi-infinite and a finite layer, or nanoribbon, with zigzag and armchair edges.

A. Zigzag semi-infinite layer

For zigzag edge orientation the boundary conditions impose that the wave function for one of the sublattice atoms must vanish [39,43,55,59]. The matrices that encode such microscopic boundary conditions for border of A and B atoms are, respectively,

$$\check{\tau}_A = \begin{pmatrix} 1 & 0 \\ 0 & 0 \end{pmatrix}, \quad \check{\tau}_B = \begin{pmatrix} 0 & 0 \\ 0 & 1 \end{pmatrix}. \tag{47}$$

For the semi-infinite layer, we can use either atom type to define the perturbation potential $\check{V}(x_a)$ at position x_a. Note that the boundary conditions defined by the matrices $\check{\tau}_A$ and $\check{\tau}_B$ cause the perturbation potential $\check{V}(x_a)$ to maintain the translational invariance along the y direction.[1] Following the method described above, we reach Eqs. (23) and (24) at each side of x_a.

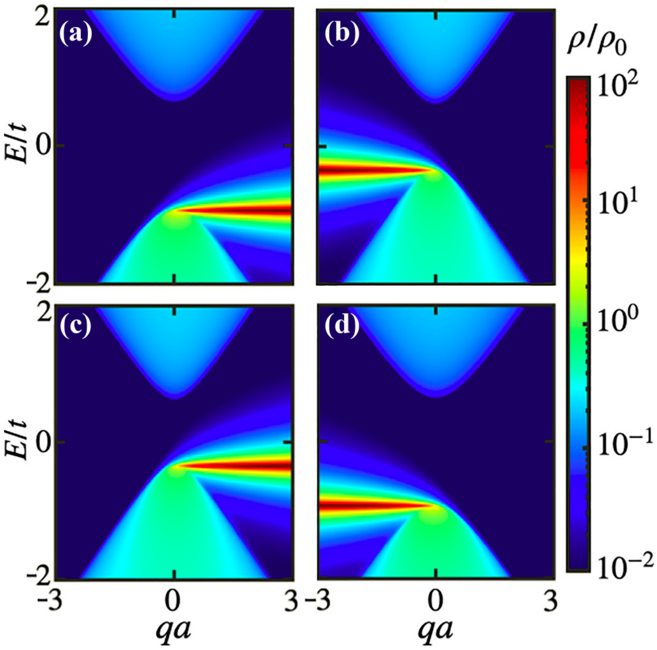

FIG. 2. Spectral density of states at the edge of a semi-infinite monolayer of TMD, where $\Delta = 1.28t$ and $\lambda_{SO} = 0.15t$. Panels (a) and (b) represent spin-up valleys (a) K' and (b) K, while panels (c) and (d) correspond to spin down (c) K' and (d) K.

To fully characterize the semi-infinite GF, we must define the scattering amplitudes, see Eqs. (25) and (26), which yield $\hat{r}_a^{+-} = (\hat{\tau}_a^{++})^{-1}\hat{\tau}_a^{+-}$. For instance, $\hat{\tau}_a^{++}$ (a scalar for zigzag termination) corresponds to the projection of $\check{\tau}$ onto the right-propagating states and their transposed counterparts. As a result, for border type A (B) we get $\hat{r}_{a,s\eta}^{+-} = \hat{r}_{s\eta}^{+-}(x_a) = -(+)e^{\pm i\alpha_{s\eta}}e^{-2ik_{s\eta}x_a}$. The phase factor $e^{-2ik_{s\eta}x_a}$ is irrelevant for the semi-infinite case, but very important for the finite layer. Plugging $\hat{r}_{s\eta}^{+-}(x_a)$ into Eq. (23), we find $\rho_{s\eta} = \mathrm{Im}(iN_{s\eta}^2 e^{i\alpha_{s\eta}})/(\pi\hbar v_F)$ for A-type termination, and $\rho_{s\eta} = \mathrm{Im}(ie^{i\alpha_{s\eta}}/N_{s\eta}^2)/(\pi\hbar v_F)$ for border B. In both cases,

$$N_{s\eta}^2 = \frac{\sqrt{E-\mu_{s\eta}-m_{s\eta}}}{\sqrt{E-\mu_{s\eta}+m_{s\eta}}}, \tag{48}$$

see more details in Sec. D.

We now illustrate different applications of the semi-infinite GF associated with Eq. (40). By setting $\Delta = 1.28t$ and $\lambda_{SO} = 0.15t$, the Hamiltonian of Eq. (40) describes the low-energy electronic excitations of a semiconductor TMD like, e.g., WSe$_2$ (usually, $t \approx 1.4$eV [56,58,58,60]). We plot in Fig. 2 the spectral density of states, Eq. (45), at the zigzag edge, for each valley and spin configuration. Similarly, choosing $\lambda_{so} = 0.0033t$ and $\Delta = 0$, we obtain the edge dispersion of a germanene layer with one zigzag edge, see Fig. 3. While the TMD features a large, semiconducting gap of the order of t, the germanene gap is much smaller, two orders of magnitude, as it corresponds to a semimetallic material. Moreover, a finite intrinsic gap Δ combined with the spin-orbit gap λ_{SO} in the TMD, yields a strong asymmetry in the resulting band gap for

---

[1] The zigzag and armchair boundary conditions encoded in the matrices $\check{\tau}$ describe such terminations with atomic precision [39,43]. Reference [43] further demonstrated that including these matrices in Eq. (10) is necessary to recover the tight-binding bulk Green's function from the semi-infinite solutions in both zigzag and armchair terminations.

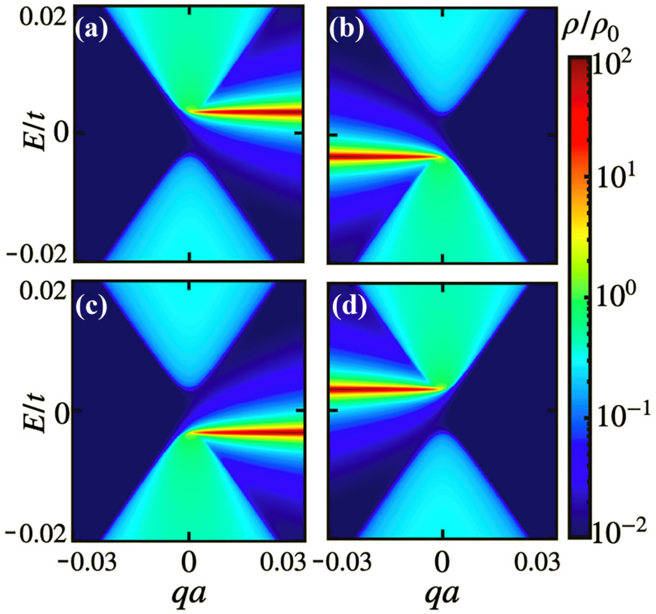

FIG. 3. Spectral density of states at the edge of a semi-infinite zigzag germanene monolayer. Panels (a) and (b) represent spin-up valleys (a) K' and (b) K, while panels (c) and (d) correspond to spin down (c) K' and (d) K. $\Delta = 0$ and $\lambda_{SO} = 0.0033t$.

the different spin-valley configurations. By contrast, the band gap of the germanene zigzag layer, with $\Delta = 0$, is only due to the spin-orbit coupling and is thus smaller and symmetric. We note that the wave number q is defined around a given valley, e.g., K' in Fig. 2(a) and K in Fig. 2(b).

The zigzag termination features an edge state in both materials, with a dispersion connecting both valleys [61]. However, while the edge state trivially connects the different valence bands for the TMD, Fig. 2, it couples conduction and valence bands for the germanene case, Fig. 3. As a result, the semi-infinite zigzag germanene layer displays two edge states that cross the Fermi energy with opposite velocities, meaning that germanene is a topological insulator [31,62,63]. We explore in Fig. 4 the decay of the edge state inside the semi-infinite layer by computing the spectral density of states at different positions away from the zigzag edge. The edge state has almost completely disappeared a few unit cells away from the edge. As we continue inside the layer, more bands appear in the spectrum, until it is almost continuum-like in the bulk case.

B. Zigzag nanoribbon

The GF for the zigzag nanoribbon, or finite layer with two zigzag edges, is obtained from Eq. (37), see Sec. C for a detailed calculation. We now highlight the main steps in its derivation for the Hamiltonian in Eq. (40). Importantly, the geometry of the zigzag nanoribbon is such that the two edges at x_a and x_b must belong to different A-B atoms, see Fig. 1. For simplicity, we now assume that $x_a < x_b$ is made of A atoms. To fully characterize the nanoribbon GF, we must first obtain the scattering amplitudes forming Eqs. (38) and (39). With our choice of atomic terminations for the zigzag nanoribbon, we have $\hat{r}^{+-}_{s\eta}(x_{a(b)}) = -(+)\mathrm{e}^{+(-)i\alpha_{s\eta}}\mathrm{e}^{-2ik_{s\eta}x_{a(b)}}$ from the semi-infinite case.

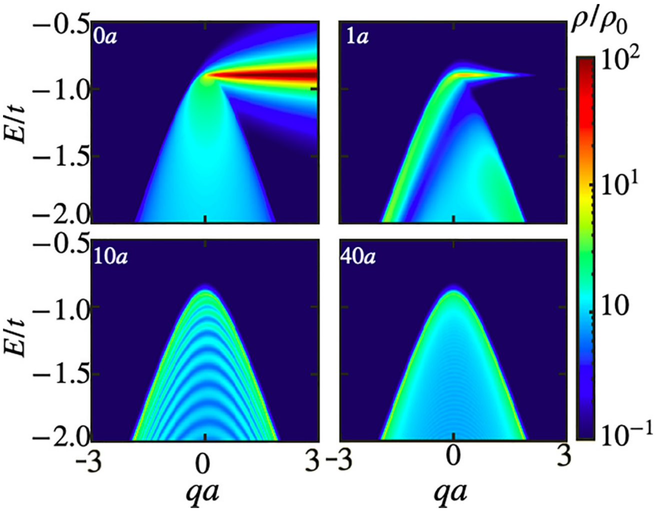

FIG. 4. Spectral density of states for spin-up, K' valley valence band of a semi-infinite zigzag TMD monolayer, at different distances from the edge. The parameters in this case are the same as in Fig. 2.

Analogously, we get $\hat{r}^{-+}_{s\eta}(x_{a(b)}) = -(+)\mathrm{e}^{-(+)i\alpha_{s\eta}+2ik_{s\eta}x_{a(b)}}$. As a result, we obtain the local GF at the A-type zigzag edge at x_a to be

$$\check{G}^{>}_{ab}(x_a, x_a) = \begin{pmatrix} 0 & -i\frac{1+\mathrm{e}^{2i(\alpha_{s\eta}+k_{s\eta}W)}}{1+\mathrm{e}^{2i(\alpha_{s\eta}+k_{s\eta}W)}} \\ 0 & -iN^2_{s\eta}\mathrm{e}^{i\alpha_{s\eta}}\frac{1-\mathrm{e}^{i2k_{s\eta}W}}{1+\mathrm{e}^{2i(\alpha_{s\eta}+k_{s\eta}W)}} \end{pmatrix}, \qquad (49)$$

with the nanoribbon width being $W = x_b - x_a$.

The local spectral density for that edge is

$$\rho(x_a) = \frac{1}{\pi\hbar v_F}\,\mathrm{Re}\left(\frac{N^2_{s\eta}\mathrm{e}^{i\alpha_{s\eta}}(1-\mathrm{e}^{i2k_{s\eta}W})}{1+\mathrm{e}^{2i(\alpha_{s\eta}+k_{s\eta}W)}}\right). \qquad (50)$$

When $W \to \infty$, the result in Eq. (50) is equal to the semi-infinite case.

In Fig. 5, we compare the edge spectral density for a TMD [Fig. 5(a)] and a germanene [Fig. 5(b)] zigzag nanoribbon.

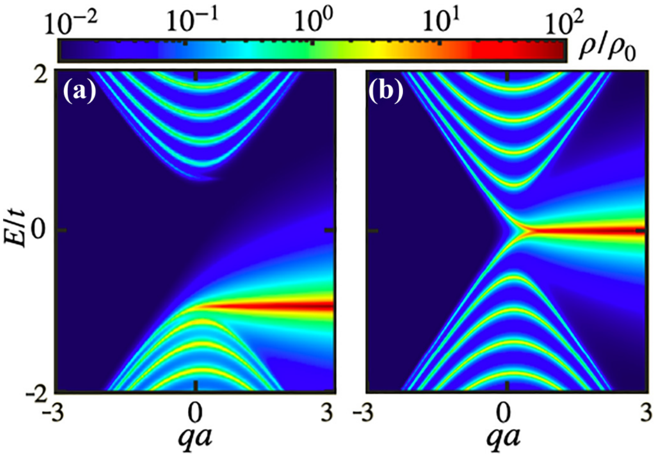

FIG. 5. Edge spectral density of a zigzag nanoribbon of (a) TMD and (b) germanene. In both cases, $W/a = 4$, and the density is computed for spin-up electrons at valley K'. The parameters, in this case, are the same as in Figs. 2 and 3.

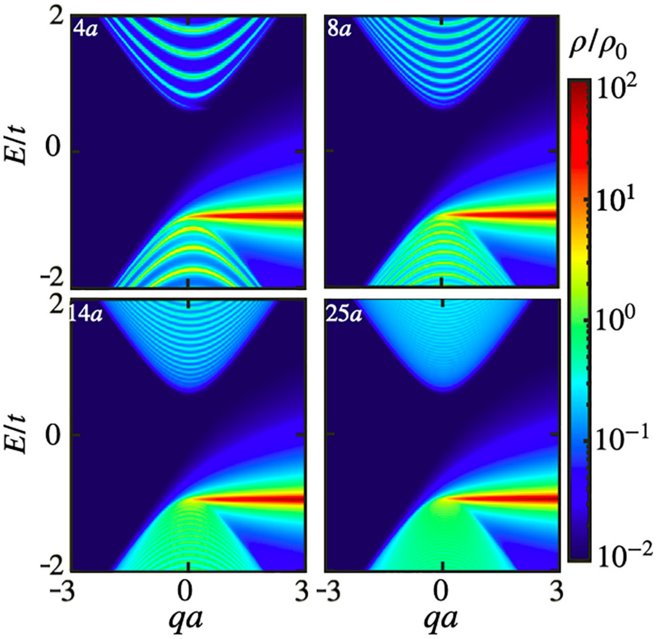

FIG. 6. Evolution of the edge spectral density of a TMD zigzag nanoribbon with the width W. All cases correspond to spin-up electrons at valley K'. The parameters, in this case, are the same as in Fig. 2.

The finite-size effect is manifested in the appearance of periodic subbands, with periodicity determined by the nanoribbon width W. Like in the semi-infinite layer, Figs. 2 and 3, the wave vector q is defined around one valley (K'). The effect of the finite width on the subband periodicity is clearly shown in Fig. 6, where we plot the edge spectral density for valley K' of a TMD zigzag nanoribbon with different widths. As the width W increases, there are more subbands per energy unit, until an almost continuum is recovered for large W. Notice that the plots show roughly the same number of subbands as unit cells form the nanoribbon width, i.e., $4a$, $8a$, etc.

Figure 7 summarizes the obtained spectral properties of zigzag germanene, Fig. 7(a), and TMDs, Fig. 7(c), showing the lowest energy spin-valley bands and the dispersion of the edge states (red and blue lines) in full momentum space including both valleys. The edge states feature trivial and nontrivial topology for TMDs and germanene, respectively. Notice the important inversion of the lowest-energy bands when the nanoribbon edge type is changed from A to B in Fig. 7(a), described by Eq. (50) changing $N_{s\eta}^2 \to 1/N_{s\eta}^2$. The effect of the termination on the band at edge state shape is encoded in the parameter $N_{s\eta}$, Eq. (48), which is inverted when the termination changes. We also sketch the lowest band dispersion for armchair germanene, Fig. 7(b), and TMD, Fig. 7(d). We explore this edge termination in more detail below.

VI. DIRAC SYSTEM WITH ARMCHAIR EDGES

In contrast with the zigzag termination that does not mix valleys, the armchair edge mixes the valley degree of freedom and thus requires a description that explicitly takes this into account. Note that the valleys for the armchair orientation are located at $\mathbf{k} \to (\pm K, 0)$, in the direction orthogonal to the conserved momentum $k_y \to q$, see Fig. 1(a).

As we did before, we start with a general Dirac Hamiltonian, valid for different graphene-like materials like germanene and TMDs, now explicitly expressed in the valley subspace as

$$\check{H}_s = \begin{pmatrix} \hat{H}_{sK} & 0 \\ 0 & \hat{H}_{sK'} \end{pmatrix}, \tag{51}$$

with $s = \pm$ the (degenerate) spin index and

$$\hat{H}_{s\eta}(\mathbf{k}) = \mu_{s\eta}\hat{\sigma}_0 + \hbar v_F(q\hat{\sigma}_y - \eta k\hat{\sigma}_x) + m_{s\eta}\hat{\sigma}_z, \tag{52}$$

with the same parameters as Eq. (40). The full Hamiltonian $\check{H}_s$ spawns in valley-sublattice 4×4 space [$N = 2$ in Eqs. 2, 3, and 19] and the reduced-space matrices denoted by $.\hat{.}.$ now

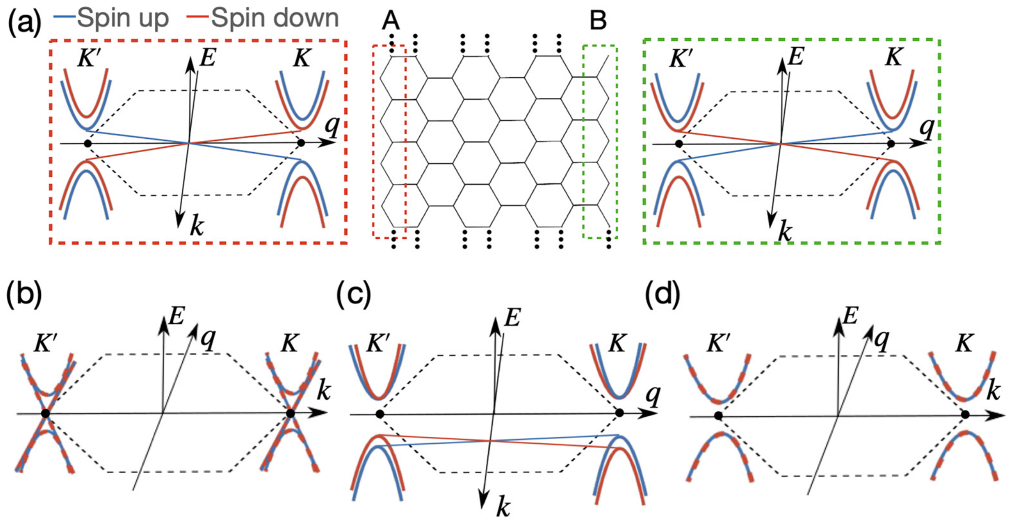

FIG. 7. Summary of the different band dispersions for TMD and germanene nanoribbons. (a) Sketch of the honeycomb lattice of a zigzag nanoribbon (middle) and band dispersion for the A (left in red) and B (right in green) type of terminations, for germanene nanoribbons. (b) Edge electronic band structure for armchair germanene. Edge electronic bands of a TMD nanoribbon with (c) zigzag or (d) armchair edges.

have dimension 2×2. The solutions of Eq. (51) are spinors in the valley subspace, $\Psi_s = (\psi_{sK}, \psi_{sK'})^T$, with each $\psi_{s\eta}$ an eigenstate of Eq. (52), see more details in Sec. D. Owing to the spin degeneracy, for simplicity we omit the spin index s in the wave functions and GFs, e.g., $\psi_{sK} \rightarrow \psi_K$. The orthogonal and transposed states are again calculated following Eqs. (4) and (9) with

$$\check{\alpha}_x = \begin{pmatrix} \hat{\sigma}_x & 0 \\ 0 & -\hat{\sigma}_x \end{pmatrix}, \quad \check{\gamma} = \begin{pmatrix} \hat{\sigma}_z & 0 \\ 0 & -\hat{\sigma}_z \end{pmatrix}. \tag{53}$$

A. Armchair semi-infinite layer

The armchair edge contains atoms of both sublattices, A and B, see Fig. 1. The armchair termination requires vanishing the wave function on both sublattices, so it is not necessary to specify the edge type as for zigzag terminations [39,43,59]. However, the boundary conditions for an armchair edge mix the valley K and K' and, thus, must be defined in the valley subspace as

$$\check{\tau} = \begin{pmatrix} \hat{\sigma}_x & \hat{\sigma}_x \\ \hat{\sigma}_x & \hat{\sigma}_x \end{pmatrix}. \tag{54}$$

As before, the edge GF for a semi-infinite layer is given by Eq. (23), which, when evaluated at the edge ($x = x_0$), adopts the form

$$\begin{aligned} &\check{G}^{<}_{RR}(x_0, x_0) \\ &= \begin{pmatrix} \hat{M}^{--}_{KK} + r^{+-}_{KK}\hat{M}^{+-}_{KK} & r^{+-}_{KK'}\hat{M}^{+-}_{KK'} \\ r^{+-}_{K'K}\hat{M}^{+-}_{K'K} & \hat{M}_{K'K'} + r^{+-}_{K'K'}\hat{M}^{+-}_{K'K'} \end{pmatrix}, \end{aligned} \tag{55}$$

with

$$\hat{M}^{\epsilon\epsilon'}_{nm} = \psi^{\epsilon}_{n}\left(\bar{\psi}^{\epsilon'}_{m}\right)^T, \tag{56}$$

$n, m = K, K'$ labeling the valleys, and $\epsilon, \epsilon' = +, -$ for, respectively, left- and right-propagating states, see Eq. (3) and Fig. 1.

The key ingredients are again the scattering amplitudes $\hat{r}^{+-} = (\hat{\tau}^{++})^{-1}\hat{\tau}^{+-}$ and $\hat{r}^{-+} = (\hat{\tau}^{--})^{-1}\hat{\tau}^{-+}$. Importantly, these 2×2 matrices are now defined in the valley subspace, and, within that subspace, every element corresponds to a projection into a specific valley index. For instance, the element $\hat{r}^{+-}_{KK'}$ of $\hat{r}^{+-}$ corresponds to the reflection amplitude for a state incident from the right ($x < x_0$) on valley K that backscatters to the left into valley K'. Defining the scalars $h^{\epsilon\epsilon'}_{nm} = \tilde{\psi}^{\epsilon\dagger}_{n}\psi^{\epsilon'}_{m}$, we find that $\hat{r}^{+-}_{KK} = h^{++}_{KK'}/h^{-+}_{KK'}$. The other elements are computed in a similar way, as shown in Sec. D.

With these simplifications, the spectral density of states reads (see more details in Sec. D)

$$\rho_s(E, q) = \frac{4}{\pi\hbar v_F}\,\mathrm{Re}\left(\frac{N^2N'^2(1 + \mathrm{e}^{i(\alpha_s-\alpha'_s)})}{N^2\mathrm{e}^{i\alpha_s} + N'^2\mathrm{e}^{-i\alpha'_s}}\right). \tag{57}$$

Here, we defined $N \equiv N_{sK}$ and $N' \equiv N_{sK'}$, following Eq. (48) evaluated for valley K and K', respectively. Analogously for α_s and α'_s with Eq. (44).

We plot the edge spectral density in Figs. 8(a) and 8(b) for a germanene and a TMD semi-infinite armchair layer, respectively. The topology of germanene is now manifested by a gapless state closing the, otherwise, small spin-orbit gap. The TMD, by contrast, presents a large semiconducting gap, like for the zigzag case. The main difference for the armchair termination is that the bands are spin symmetric, but display a small asymmetry with the conserved momentum q. Both effects stem from the symmetrization imposed by the armchair edge after combining the different spin-valley bands.

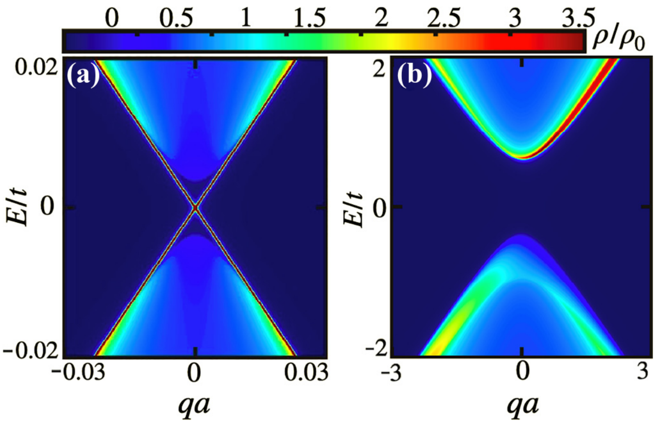

FIG. 8. Edge spectral density of states for a semi-infinite armchair layer of (a) germanene and (b) and TMD. The parameters, in this case, are the same as in Figs. 2 and 3.

The main feature about the armchair termination, that different valleys are mixed on scattering, can be better understood by checking the specific inter- and intravalley scattering amplitudes. We show in Fig. 9 the scattering coefficient for an incident electron from valley K (blue and red solid lines) and K' (green and black dashed lines) into the same or the opposite valley. For simplicity, we only show the normal incident case ($q = 0$), but similar results are obtained for any incident angle. For germanene (left panel), intervalley scattering is dominant (red and green lines), except for energies very close to the gap edge. This behavior has been previously reported for graphene [11,64]. Both inter- and intravalley coefficients are symmetric with respect to the energy, as the spin-valley bands are also symmetric, see Fig. 7. The strong asymmetry in the spin-valley bands for the TMDs (right panel) results in an intervalley scattering that is very asymmetric with the energy, with small energy windows close to the edge of the valence and conduction bands where intravalley scattering is perfect since the intervalley one is forbidden.

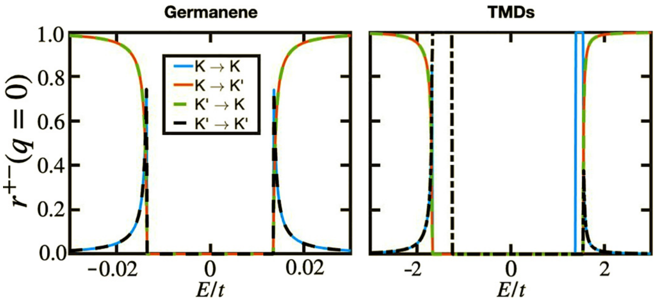

FIG. 9. Electron reflection probabilities at normal incidence ($q = 0$) in the armchair edge of a semi-infinite layer of germanene and TMD, showing intravalley (blue and black) and intervalley (red and green) scattering probabilities. The parameters, in this case, are the same as in Figs. 2 and 3.

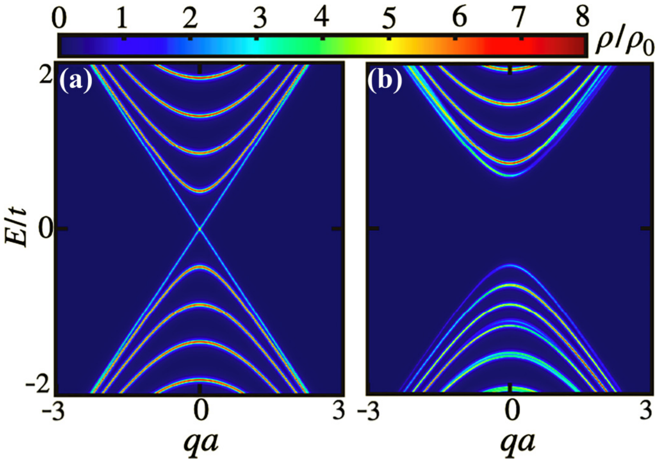

FIG. 10. Edge spectral density of states for a finite armchair nanoribbon of (a) germanene or (b) TMD. For both cases the width is six unit cells. The parameters, in this case, are the same as in Figs. 2 and 3.

B. Armchair nanoribbon

The nanoribbon GF associated with the Hamiltonian in Eq. (51) spawns in a combined spin-valley-sublattice space. Being spin-degenerate, we can focus on its 4×4 valley-sublattice structure and, within it, describe the valley-projected 2×2 matrix elements

$$\hat{G}^{>}_{nm}(x,x') = \sum_{\varepsilon,\varepsilon'=\pm} f_n^{\varepsilon}(x) f_m^{\epsilon'}(x') \hat{r}_{nm}^{>,\varepsilon\varepsilon'} \hat{M}_{nm}^{\varepsilon\varepsilon'}. \tag{58}$$

Here, $f_n^{\varepsilon}(x) = \mathrm{e}^{i(K_n+\varepsilon k_n)x}$, with $K_n = K, K'$ and $k_n = k_s, k_s'$. The matrices $\hat{M}_{nm}^{\varepsilon\varepsilon'}$ are defined in Eq. (56) and the reflection matrices according to Eq. (39). See more details in Sec. D.

We plot the spectral density of states for an armchair nanoribbon of germanene and TMD in Figs. 10(a) and 10(b), respectively, for a width of six unit cells. As expected, we observe the band discretization in both cases and the topological edge state for the germanene nanoribbon. The gapless edge state in the germanene nanoribbon of width $W = 6a$ featured in Fig. 10(a) stems from a topological phase. However, the gap can reopen due to a trivial geometrical effect arising from the interference of intravalley reflection processes at the nanoribbon edges. For clarity, we compute for two different widths, $W/a = 8$ and 9, the spectral density of states at the armchair edge of TMD and germanene nanoribbons in, respectively, Figs. 11 and 12. This geometric effect has been previously studied in graphene nanoribbons [39,43,65].

While semi-infinite germanene layers clearly feature topological edge states, see Fig. 8(a), we find that the edge state only appears when the nanoribbon width is a multiple of three, $W/a = 3n$ with integer n, see Figs. 11 and 12, and only for the germanene case since the semiconducting gap of the TMD completely suppresses this effect. Consequently, the topology in germanene armchair nanoribbons is only revealed when the geometric phase is removed. Indeed, the trivial gaps that open for $W/a \neq 3n$ exponentially decrease with the width. We show this effect in Fig. 13 by plotting the lowest energy level E_0 at the edge of a germanene nanoribbon as a function of the ribbon width. The zero energy solutions every three unit cells represent the topological edge states, while the trivial gaps for

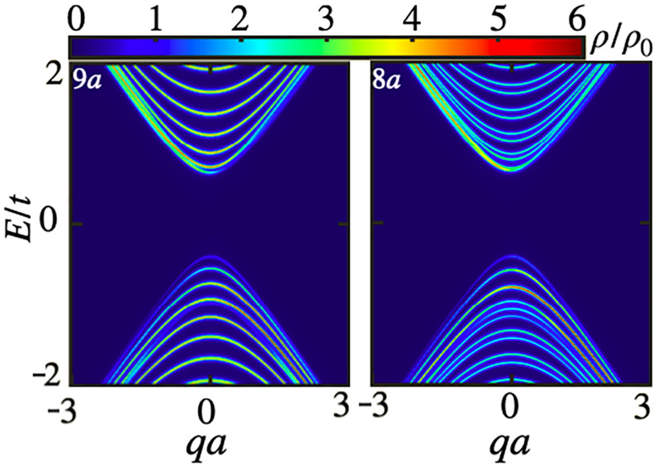

FIG. 11. Spectral density of states at the armchair edge of TMD nanoribbons for $W/a = 8$ (right) and $W/a = 9$ (left). The parameters, in this case, are the same as in Fig. 2.

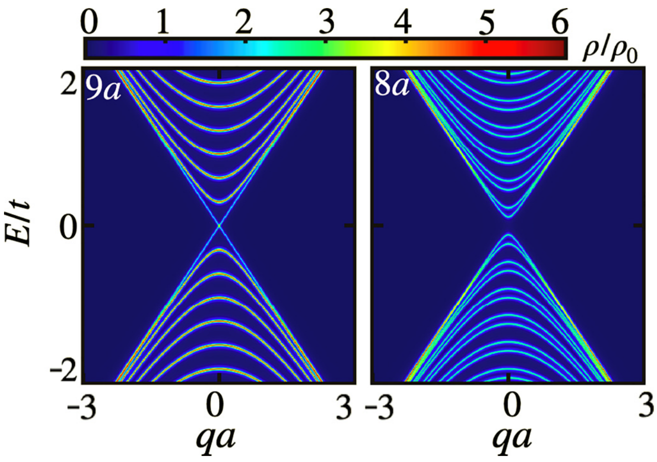

FIG. 12. Spectral density of states at the armchair edge of germanene nanoribbons for $W/a = 8$ (right) and $W/a = 9$ (left). The parameters, in this case, are the same as in Fig. 3.

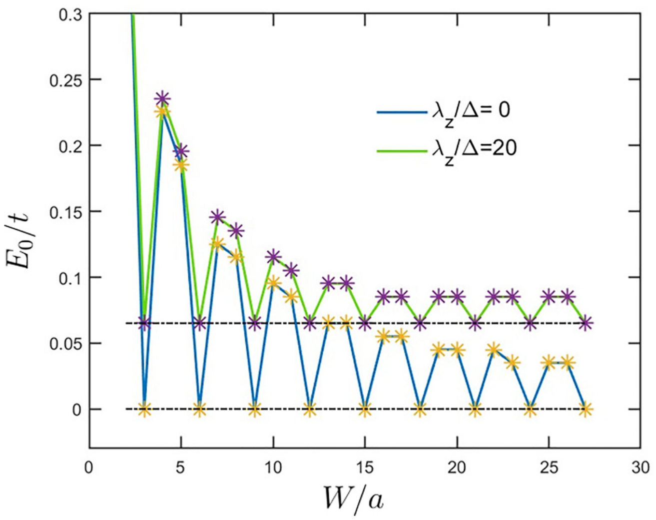

FIG. 13. Lowest energy levels for armchair nanoribbons as a function of the nanoribbon width with (green) and without (blue) external electric field λ_z.

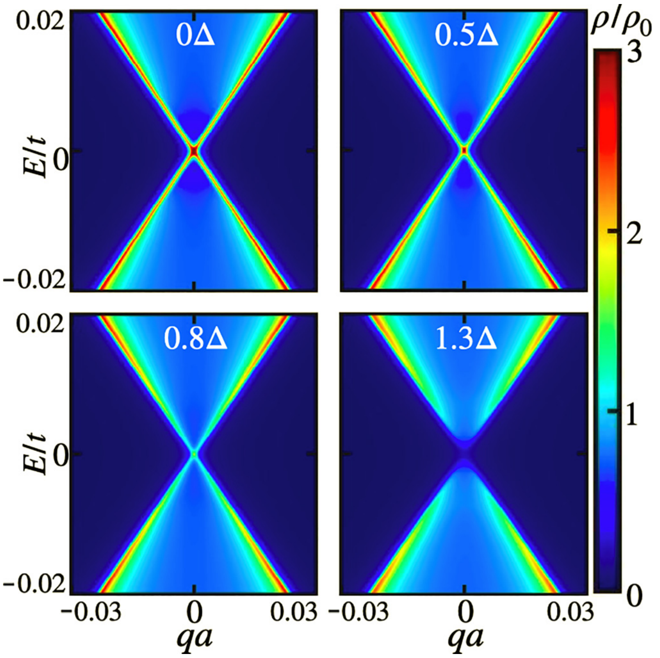

FIG. 14. Spectral density of states at the armchair edge of a semi-infinite germanene layer, for $\lambda_z/\Delta = 0$, 0.5, 0.8, and 1.3. The parameters in this case are the same as in Fig. 3.

the other multiplicities quickly decay to close the gap in the semi-infinite limit ($W \to \infty$).

VII. GERMANENE GAP MANIPULATION

Using the GF formalism introduced in Secs. II–IV, we have successfully described the electronic band structure of bulk, semi-infinite, and finite layers of graphene-like materials. These GF methods give us access to the spectral density of states and can easily take into account extra parameters in the Hamiltonian. In this section, we showcase this by studying the effect of an external perpendicular electric field on the electronic and topological properties of a germanene layer. Germanene is a topological insulator with a topological invariant characterized by a $\mathcal{Z}_2$ index [35], which corresponds to a nontrivial phase in the absence of an electric field analogous to a graphene layer with induced spin-orbit coupling [66]. Here, for simplicity, we only consider a semi-infinite armchair layer where the gap closes at the center of the Brillouin zone for $q \approx 0$, see Fig. 8(a). Our results below can be extended to zigzag terminations noting, however, that the closing of the gap takes place between valleys as depicted in Fig. 7. As introduced in Eqs. (40) and (52), the parameter λ_z represents the effect of such an external field perpendicular to the layer.

The semi-infinite armchair germanene layer features a topological edge state crossing the Fermi energy [Fig. 8(a)]. For comparison, we reproduce this result in the top-left panel of Fig. 14 ($\lambda_z = 0$) and proceed to study the evolution of the edge state for finite λ_z. As the external electric field increases, the gap closes, removing the edge state ($\lambda_z/\Delta \simeq 0.8$), and the layer becomes semimetallic. By further increasing the field, the gap reopens into a trivial, semiconducting phase, i.e., without edge state. Such a topological gap manipulation has been recently measured [67].

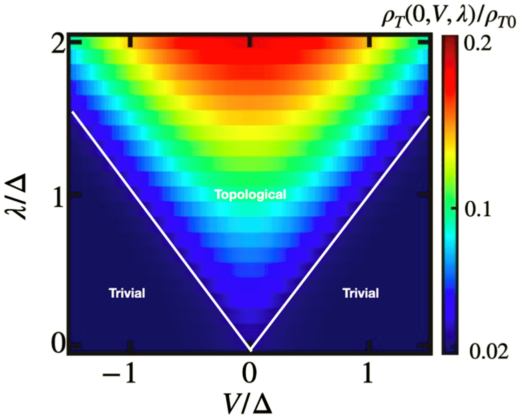

FIG. 15. Zero-energy density of states of a semi-infinite armchair germanene layer as a function of an external electric field and the spin-orbit coupling. The parameters, in this case, are the same as in Fig. 3.

The gap induced by the external electric field is thus competing with the topological gap from the spin-orbit coupling, λ_{SO} in Eq. (52). We explore such interplay in Fig. 15 by computing the zero-energy LDOS as a function of both λ_z and λ_{SO}. The semi-infinite armchair germanene layer is topologically nontrivial (trivial) when $\lambda_z < \lambda_{SO}$ ($\lambda_z > \lambda_{SO}$), with critical lines at $\lambda_z = \lambda_{SO}$.

In a finite-size system there is a width-dependent geometrical effect on armchair nanoribbons, see Sec. VI B, which persists in the trivial regime. However, the lowest energy level when the geometric phase has been removed for $W/a = 3n$ is no longer zero, like in the nontrivial case, but determined by the semiconducting gap, see green line with $\lambda_z \neq 0$ in Fig. 13. Although the field required to close the gap in armchair nanoribbons slightly depends on the width, for sufficiently wide nanoribbons this variation with the width becomes negligible.

The spectral properties of germanene and other graphene-like materials are of great interest after the recent development of gap engineering methods [67–69]. The GF methods developed here provide a useful approach for the study of their spectral and topological properties while tuning several physical parameters of the system.

VIII. CONCLUSIONS

We have developed a general and analytic method for computing the microscopic Green's functions of a two-dimensional Dirac Hamiltonian with atomic-scale boundary conditions. Our approach is thus valid for honeycomb lattices with atomically well-defined zigzag and armchair edges, and contains all the relevant information about the scattering processes that take place at these edges, including spin, sublattice (from the honeycomb structure), and valley degrees of freedom.

We tested our Green's function formalism by computing the spectral and topological properties of several well-known Dirac materials, like semimetal germanene and semiconducting transition metal dichalcogenides. Our approach allowed us to characterize bulk (infinite two-dimensional layer), semi-infinite, and finite layers. The zigzag termination resulted in the emergence of localized edge states, which have a topological nature in germanene samples [35], and are affected, in nanoribbons (finite layers), by the spectral quantization resulting from the finite ribbon length.

We go beyond previous works [32] showing that the topological properties of germanene are maintained for armchair terminations. We also showed how the topological gap for this material can be manipulated by an external electric field, which could be helpful for field effect transistor using germanene or silicene. This effect in silicene has been recently measured [70], and its potential use as a topological field effect transistor has also been theoretically explored [35].

The analytical formalism presented here aligns with current efforts to explore and engineer novel two-dimensional junctions with interesting quantum applications [71], as it paves the way for the exploration of exotic electronic phases in nanoscale junctions based on Dirac materials, including important effects like edge terminations, valley-dependent scattering, and finite-size effects.

In general, our approach provides an analytical alternative, with low computational cost, to simulate the low-energy electronic properties of graphene-like materials at the atomic level. It is straightforward to generalize it to study quantum transport in junctions with atomic-scale electric contacts [72–75], or to include magnetic or superconducting orders [76]. In addition, the analytical expressions computed here offer great flexibility to include several effects, such as band-gap engineering, external fields, and even light-matter interactions [68,69,77–79].

ACKNOWLEDGMENTS

J.T.-I. and W.J.H. acknowledge support from the Universidad Nacional de Colombia, project No. 57522. P.B. acknowledges support from the Spanish CM "Talento Program" project No. 2019-T1/IND-14088 and the Agencia Estatal de Investigación project No. PID2020-117992GA-I00 and No. CNS2022-135950.

APPENDIX A: ITERATIVE METHOD

In this section, we obtain $\check{Q}^>(x)$ given in Eq. (15) following an iterative method. First, we start using Eq. (13) with $x < x'$ in the definition of the GF,

$$\check{G}^<_a(x,x') = \check{g}^<(x,x') + \check{g}^>(x,x_a)U_a\check{t}_a\check{G}^<_{RR}(x_a,x'). \quad \text{(A1)}$$

Here, $\check{G}^<_{RR}(x_a,x')$ is given by Dyson's equation, Eq. (12), as

$$\check{G}^<_{RR}(x_a,x') = [1+\check{Q}^>(x_a)]\check{g}^<(x_a,x'). \quad \text{(A2)}$$

Substituting into Eq. (A1) we get

$$\begin{aligned}\check{G}^<_{RR}(x,x') =& \check{g}^<(x,x') + \check{g}^>(x,x_a) \quad \text{(A3)}\\ &\times U_a\check{t}_a(1+\check{Q}^>(x_a))\check{g}^<(x_a,x').\end{aligned}$$

Comparing Eq. (A3) with Eq. (12), namely,

$$\check{G}^{RR,<}_a(x,x') = \check{g}^<(x,x') + \check{Q}^>(x)\check{g}^<(x_a,x'),$$

we obtain the following equation for $\check{Q}^>(x)$:

$$\check{Q}^>(x) = \check{g}^>(x,x_a)U_a\check{t}_a + \check{g}^>(x,x_a)U_a\check{t}_a\check{Q}^>(x_a). \quad \text{(A4)}$$

We then solve Eq. (A4) recursively to find

$$\check{Q}^>(x) = U_a\check{g}^>(x,x_a)\check{t}_a\sum_{p=0}U_a^p(\check{g}^>(0)\check{t}_a)^p. \quad \text{(A5)}$$

APPENDIX B: SCATTERING MATRIX

We now derive the expression and general properties of the scattering matrix in Eq. (25). To define the scattering problem, we consider a potential barrier at $x = x_a$. Incoming states from the left (right) of the barrier are $\psi^+_m(x)$ with amplitudes a^+_m [$\psi^-_m(x)$ with a^-_m], which are solutions of Eq. (2). In the absence of a potential barrier, a general unperturbed scattering state reads

$$\psi_0(x) = \sum_{m,\varepsilon} a^\varepsilon_m\psi^\varepsilon_m(x). \quad \text{(B1)}$$

In the presence of the barrier potential, the perturbed state to the left or right of the barrier is obtained using Dyson's equation as

$$\psi_{L(R)}(x) = \psi_0(x) + \check{Q}^{<(>)}(x)\psi_0(x_a), \quad \text{(B2)}$$

with $\psi^\varepsilon_m(x) = \psi^\varepsilon_m f^\varepsilon_m(x)$ and $f^\varepsilon_m(x) = e^{i\varepsilon k_m x}$.

Owing to the translational invariance along the x direction, we proceed taking $x_a = 0$ without loss of generality. For simplicity, we also define $\psi_R(0) = \psi_R$ and $\psi_0(0) = \psi_0$ and obtain

$$\begin{aligned}\psi_R &= [1+\check{Q}^>(0)]\psi_0\\ &= \left(1+\sum_{n,m,\varepsilon}\left(\hat{r}^{+\varepsilon}_a\right)_{nm}\hat{P}^{+\varepsilon}_{nm}\right)\sum_{m',\varepsilon'}a^{\varepsilon'}_{m'}\psi^{\varepsilon'}_{m'}\\ &= \sum_{m,\varepsilon}a^\varepsilon_m\psi^\varepsilon_m + \sum_{n,m,\varepsilon}\left(\hat{r}^{+\varepsilon}_a\right)_{nm}a^\varepsilon_m\psi^+_m, \quad \text{(B3)}\end{aligned}$$

where we have used that $\hat{P}^{+\varepsilon}_{nm}\psi^{\varepsilon'}_{m'} = \delta_{\varepsilon,\varepsilon'}\delta_{m,m'}\psi^{\varepsilon'}_{m'}$. Summing over ε we get

$$\psi_R = \sum_m a^-_m\psi^-_m + \sum_n b^+_n\psi^+_n, \quad \text{(B4)}$$

with b^+_n being the outgoing scattering amplitudes,

$$b^+_n = \sum_m(\hat{r}^{+-}_a)_{nm}a^-_m + \sum_m(\hat{t}^{++}_a)_{nm}a^+_m. \quad \text{(B5)}$$

Here, we have defined the transmission amplitudes as the elements of the following matrix:

$$\hat{t}^{++}_a = \hat{1} + \hat{r}^{++}_a, \quad \text{(B6)}$$

which allows us to rewrite Eq. (B5) as

$$\mathbf{b}^+ = \hat{r}^{+-}_a\mathbf{a}^- + \hat{t}^{++}_a\mathbf{a}^+, \quad \text{(B7)}$$

with

$$\mathbf{b}^{+T} = (b_1, b_2, \dots, b_N)^T, \quad \text{(B8)}$$

$$\mathbf{a}^{+T} = (a_1, a_2, \dots, a_N)^T. \quad \text{(B9)}$$

The perturbed scattering state to the left of the barrier is obtained analogously as

$$\psi_L(0) = \sum_m a^+_m\psi^+_m + \sum_n b^-_n\psi^-_n, \quad \text{(B10)}$$

with

$$\mathbf{b}^{-}=\hat{r}_a^{-+}\mathbf{a}^{+}+\hat{t}_a^{--}\mathbf{a}^{-}, \tag{B11}$$

and

$$\hat{t}_a^{--}=\hat{1}+\hat{r}_a^{--}. \tag{B12}$$

Combining the previous results, we define the scattering matrix $\hat{S}$ as

$$\mathbf{b}=\check{S}\mathbf{a}, \tag{B13}$$

with

$$\mathbf{b}=\begin{pmatrix}\mathbf{b}^{+}\\ \mathbf{b}^{-}\end{pmatrix},\quad \mathbf{a}=\begin{pmatrix}\mathbf{a}^{+}\\ \mathbf{a}^{-}\end{pmatrix}. \tag{B14}$$

Note that in the usual definition of the scattering matrix the reflection amplitudes are in the diagonal, which results from taking $\mathbf{b}^T=(\mathbf{b}^{-T},\mathbf{b}^{+T})$. In what follows, however, we use

$$\begin{aligned}\check{S}_a&=\begin{pmatrix}\hat{t}_a^{++} & \hat{r}_a^{+-}\\ \hat{r}_a^{-+} & \hat{t}_a^{--}\end{pmatrix}\\ &=\begin{pmatrix}\hat{1}+\hat{r}_a^{++} & \hat{r}_a^{+-}\\ \hat{r}_a^{-+} & \hat{1}+\hat{r}_a^{--}\end{pmatrix}\\ &=\check{1}+\check{r}_a.\end{aligned} \tag{B15}$$

We can now set the potential barrier at an arbitrary position $x_a\neq 0$ changing the scattering matrix as

$$\check{S}(x_a)=\check{f}(-x_a)\check{S}\check{f}(x_a), \tag{B16}$$

with

$$\check{f}(x_a)=\begin{pmatrix}\check{f}^{++}(x_a) & 0\\ 0 & \check{f}^{--}(x_a)\end{pmatrix}, \tag{B17}$$

and

$$\left(\hat{f}^{\varepsilon\varepsilon}\right)_{nm}(x)=\delta_{nm}\hat{f}_m^{\varepsilon}(x). \tag{B18}$$

Here, $\hat{S}(x_a)$ and $\hat{S}$ are related by a unitary transformation since $\hat{f}(-x_0)\hat{f}(x_0)=\hat{1}$.

As it is usually interpreted, **b** represents the outgoing flux and **a** the incoming one. Consequently, the probability flux to the right and left of the barrier reads

$$\begin{aligned}J_R&=v_F\sum_n(a_n^{-*}\psi_n^{-\dagger}+b_n^{+*}\psi_n^{+\dagger})\hat{\alpha}_x\sum_n(a_n^{-}\psi_n^{-}+b_n^{+}\psi_n^{+})\\ &=v_F\sum_n(|b_n^{+}|^2-|a_n^{-}|^2),\end{aligned} \tag{B19}$$

$$\begin{aligned}J_L&=v_F\sum_n(a_n^{+*}\psi_n^{+\dagger}+a_n^{-*}\psi_n^{-\dagger})\hat{\alpha}_x\sum_n(a_n^{+}\psi_n^{+}+a_n^{-}\psi_n^{-})\\ &=v_F\sum_n(|a_n^{+}|^2-|b_n^{-}|^2).\end{aligned} \tag{B20}$$

Conservation of the probability flux requires that $J_L=J_R$; therefore,

$$\sum_n(|a_n^{+}|^2-|b_n^{-}|^2)=\sum_n(|b_n^{+}|^2-|a_n^{-}|^2), \tag{B21}$$

$$\sum_n(|a_n^{+}|^2+|a_n^{-}|^2)=\sum_n(|b_n^{+}|^2+|b_n^{-}|^2), \tag{B22}$$

which we can recast in vector form as $|\mathbf{b}|^2=|\mathbf{a}|^2$. As a result, we find that

$$\mathbf{a}^{\dagger}\check{S}^{\dagger}\check{S}\mathbf{a}{=}|\mathbf{a}|^2, \tag{B23}$$

and thus,

$$\mathbf{a}^{\dagger}(\check{S}^{\dagger}\check{S}-1)\mathbf{a}=0. \tag{B24}$$

Equation (B24) proves that the scattering matrix is unitary; that is,

$$\check{S}^{\dagger}\check{S}=\check{S}\check{S}^{\dagger}=\check{1}, \tag{B25}$$

which we can recast using the reflection matrix $\check{r}$ as

$$(\check{1}+\check{r}_a)(\check{1}+\check{r}_a^{\dagger})=(\check{1}+\check{r}_a^{\dagger})(\check{1}+\check{r}_a)=\check{1}. \tag{B26}$$

APPENDIX C: NANORIBBON GREEN'S FUNCTION AND BOUND STATES

In this section we provide more details on the derivation of the nanoribbon GF, Eq. (37), and the associated bound states. For the case of two potential barriers placed at $x=x_a$ and $x=x_b>x_a$, the perturbed GF for the region between the barriers is

$$\check{G}_{ab}(x,x')=\check{G}_a(x,x')+\check{Q}^{<}(x)\check{G}_{ab}^{>}(x_b,x'), \tag{C1}$$

for $x>x'$, where

$$\begin{aligned}&\check{G}_{ab}^{>}(x,x')\\ &\quad=\frac{-i}{2\hbar v_F}\sum_{n,m,\varepsilon,\varepsilon'}f_n^{\varepsilon}(x-x_b)(\check{w}^{>})_{nm}^{\varepsilon\varepsilon'}f_m^{\varepsilon'}(x_b-x')\psi_n^{\varepsilon}\left(\bar{\psi}_m^{\varepsilon'}\right)^T,\end{aligned} \tag{C2}$$

with $\check{w}^{>}$ given by Eq. (33), see also Eq. (32).

Equation (C1) can be solved after obtaining $\check{G}_{ab}^{>}$. However, to do so, one cannot take the limit $U_b\to\infty$ and invert $\check{w}$, because the matrix $\check{\tau}$ has no inverse ($\det[\check{\tau}]=0$). To circumvent this problem, we define the matrix

$$\check{N}=\check{1}-AU_b\check{\tau}, \tag{C3}$$

with $A=-i/(2\hbar v_F)$, and

$$\check{N}=\begin{pmatrix}\hat{N}_1 & \hat{N}_2\\ \hat{N}_3 & \hat{N}_4\end{pmatrix}, \tag{C4}$$

where

$$\begin{aligned}\hat{N}_1&=\hat{1}-AU_b\hat{r}_a^{+-}(W)\hat{\tau}_b^{-+},\quad &\hat{N}_3&=-AU_b\hat{\tau}_b^{-+},\\ \hat{N}_2&=-AU_b\hat{r}_a^{+-}(W)\hat{\tau}_b^{--},\quad &\hat{N}_4&=AU_b\hat{\tau}_b^{-+}(\hat{r}_b^{-+})^{-1}.\end{aligned}$$

We can now compute the inverse of $\hat{N}$ and then take the limit $U_b\to\infty$. To do so, we use Schur complement, which, for example, is defined for submatrix $\hat{N}_4$ as

$$\hat{C}=\hat{N}_1-\hat{N}_2\hat{N}_4{}^{-1}\hat{N}_3.$$

Therefore, defining

$$\hat{r}_b^{-+}=AU_b(\hat{1}-AU_b^{--}\hat{\tau}_b)^{-1}\hat{\tau}_b^{-+},$$

we get

$$\hat{C}=\hat{1}-\hat{r}_a^{+-}(W)\hat{r}_b^{-+}, \tag{C5}$$

with $W=x_b-x_a$.

The inverse matrix of $\hat{N}$ is thus

$$\check{N}^{-1}=\begin{pmatrix}\hat{1} & 0\\ -\hat{N}_4^{-1}\hat{N}_3 & \hat{1}\end{pmatrix}\begin{pmatrix}\hat{C}^{-1} & 0\\ 0 & \hat{N}_4^{-1}\end{pmatrix}\begin{pmatrix}\hat{1} & -\hat{N}_2\hat{N}_4^{-1}\\ 0 & \hat{1}\end{pmatrix}, \tag{C6}$$

which simplifies to

$$\check{N}^{-1}=\begin{pmatrix}\hat{C}^{-1} & \hat{C}^{-1}\hat{r}_a^{+-}(W)\hat{\tau}_b^{--}\hat{r}_b^{-+}(\hat{\tau}_b^{-+})^{-1}\\ \hat{r}_b^{-+}\hat{C}^{-1} & U_b^{-1}\hat{r}_b^{-+}\hat{C}^{-1}[\hat{1}-U_b\hat{r}_a^{+-}(W)\hat{\tau}_b^{-+}]\big(\hat{\tau}_b^{-+}\big)^{-1}\end{pmatrix}. \tag{C7}$$

We can now take the limit $U_b \to \infty$, resulting in

$$\check{w}^{<}=\begin{pmatrix}\hat{C}^{-1}\hat{r}_a^{+-}(W)\hat{r}_b^{-+} & -\hat{C}^{-1}\hat{r}_a^{+-}(W)\\ \hat{r}_b^{-+}\hat{C}^{-1} & -\hat{r}_b^{-+}\hat{C}^{-1}(\hat{r}_b^{-+})^{-1}\end{pmatrix}. \tag{C8}$$

Analogously, we get

$$\check{w}^{>}=\begin{pmatrix}\hat{D}^{++} & \hat{D}^{++}\hat{r}_a^{+-}(x_a)\\ \hat{r}_b^{-+}(x_b)\hat{D}^{++} & \hat{r}_b^{-+}(x_b)\hat{D}^{++}\hat{r}_a^{+-}(x_a)\end{pmatrix}, \tag{C9}$$

with

$$\hat{D}^{++}=[\hat{1}-\hat{r}_a^{+-}(x_a)\hat{r}_b^{-+}(x_b)]^{-1}, \tag{C10}$$

$$\hat{D}^{--}=[\hat{1}-\hat{r}_b^{-+}(x_b)\hat{r}_a^{+-}(x_a)]^{-1}. \tag{C11}$$

As a result, we obtain the final form of the nanoribbon GF as

$$\check{G}_{ab}^{\lessgtr}(x,x')=\frac{-i}{2\hbar v_F}\sum_{\substack{n,m\\ \varepsilon,\varepsilon'}} f_n^{\varepsilon}(x)(\check{w}^{\lessgtr})_{nm}^{\varepsilon\varepsilon'} f_m^{\varepsilon'}(-x')\psi_n^{\varepsilon}\big(\bar{\psi}_m^{\varepsilon'}\big)^T. \tag{C12}$$

The nanoribbon's bound states are obtained from the denominator of the GF, that is, setting the inverse of $\hat{D}^{++}$ or, equivalently, $\hat{D}^{--}$, to zero. From Eq. (C10), this condition reduces to

$$\hat{r}_a^{+-}(x_a)\hat{r}_b^{-+}(x_b)=\hat{1}. \tag{C13}$$

We can interpret this condition as follows: inside the nanoribbon, the scattering state is a superposition of left and right movers, namely,

$$\psi=\sum_n(c_n^{+}\psi_n^{+}+c_n^{-}\psi_n^{-}). \tag{C14}$$

At each potential barrier, $x=x_{a,b}$, the amplitudes for left and right movers, c_n^- and c_n^+, respectively, are related by

$$c_n^{-}=\sum_m \hat{r}_{nm}^{-+}(x_b)c_m^{+}, \tag{C15}$$

$$c_n^{+}=\sum_m \hat{r}_{nm}^{+-}(x_a)c_m^{-}. \tag{C16}$$

In matrix form we have

$$\mathbf{c}^{-}=\hat{r}^{-+}(x_b)\mathbf{c}^{+}, \tag{C17}$$

$$\mathbf{c}^{+}=\hat{r}^{+-}(x_a)\mathbf{c}^{-}, \tag{C18}$$

which form the closed cycle

$$\mathbf{c}^{+}=\hat{r}^{+-}(x_a)\hat{r}^{-+}(x_b)\mathbf{c}^{+}. \tag{C19}$$

It is thus straightforward to get

$$\mathbf{c}^{+}[\hat{1}-\hat{r}^{+-}(x_a)\hat{r}^{-+}(x_b)]=\mathbf{0}, \tag{C20}$$

which corresponds to the zeros of the GF, as shown in Eq. (C13). This result shows that the nanoribbon's bound states are determined by the reflection matrices at each edge of the finite region, and can thus be obtained by the zeros of the inverse of Eq. (C10).

APPENDIX D: GREEN'S FUNCTIONS FOR DIRAC SYSTEMS WITH WELL-DEFINED EDGES

This Appendix contains the necessary definitions and supplementary calculations to derive the GF of the zigzag Hamiltonian in Eq. (40) and the armchair one in Eq. (51).

1. Zigzag Hamiltonian

The normalized eigenstates associated with Eq. (40) are

$$\psi_{s\eta}^{+}=\frac{1}{\sqrt{2\cos\alpha_{s\eta}}}\begin{pmatrix}N_{s\eta}^{-1}\mathrm{e}^{-i\frac{\alpha_{s\eta}}{2}}\\ N_{s\eta}\mathrm{e}^{i\frac{\alpha_{s\eta}}{2}}\end{pmatrix}, \tag{D1a}$$

$$\psi_{s\eta}^{-}=\frac{1}{\sqrt{2\cos\alpha_{s\eta}}}\begin{pmatrix}N_{s\eta}^{-1}\mathrm{e}^{i\frac{\alpha_{s\eta}}{2}}\\ -N_{s\eta}\mathrm{e}^{-i\frac{\alpha_{s\eta}}{2}}\end{pmatrix}, \tag{D1b}$$

$$\tilde{\psi}_{s\eta}^{+}=\frac{1}{\sqrt{2\cos\alpha_{s\eta}}}\begin{pmatrix}N_{s\eta}\mathrm{e}^{i\frac{\alpha_{s\eta}}{2}}\\ N_{s\eta}^{-1}\mathrm{e}^{-i\frac{\alpha_{s\eta}}{2}}\end{pmatrix}, \tag{D1c}$$

$$\tilde{\psi}_{s\eta}^{-}=\frac{1}{\sqrt{2\cos\alpha_{s\eta}}}\begin{pmatrix}N_{s\eta}\mathrm{e}^{i\frac{-\alpha_{s\eta}}{2}}\\ -N_{s\eta}^{-1}\mathrm{e}^{i\frac{\alpha_{s\eta}}{2}}\end{pmatrix}. \tag{D1d}$$

The corresponding transposed states are

$$\bar{\psi}_{s\eta}^{+}=\frac{1}{\sqrt{2\cos\alpha_{s\eta}}}\begin{pmatrix}N_{s\eta}^{-1}\mathrm{e}^{i\frac{\alpha_{s\eta}}{2}}\\ N_{s\eta}\mathrm{e}^{-i\frac{\alpha_{s\eta}}{2}}\end{pmatrix}, \tag{D2}$$

$$\bar{\psi}_{s\eta}^{-}=\frac{1}{\sqrt{2\cos\alpha_{s\eta}}}\begin{pmatrix}N_{s\eta}^{-1}\mathrm{e}^{-i\frac{\alpha_{s\eta}}{2}}\\ -N_{s\eta}\mathrm{e}^{i\frac{\alpha_{s\eta}}{2}}\end{pmatrix}. \tag{D3}$$

It is thus possible to write $\bar{\psi}_{s\eta}^{\epsilon T}=\psi_{s\eta}^{\epsilon\dagger}$. Next, the bulk GFs reads

$$g_{s\eta}^{<}(x,x')=\frac{\mathrm{e}^{ik_{s\eta}(x'-x)}}{2\cos\alpha_{s\eta}}\begin{pmatrix}N_{s\eta}^{-2} & -\mathrm{e}^{i\alpha_{s\eta}}\\ -\mathrm{e}^{-i\alpha_{s\eta}} & N_{s\eta}^{2}\end{pmatrix}, \tag{D4}$$

$$g_{s\eta}^{>}(x,x')=\frac{\mathrm{e}^{ik_{s\eta}(x-x')}}{2\cos\alpha_{s\eta}}\begin{pmatrix}N_{s\eta}^{-2} & \mathrm{e}^{-i\alpha_{s\eta}}\\ \mathrm{e}^{i\alpha_{s\eta}} & N_{s\eta}^{2}\end{pmatrix}. \tag{D5}$$

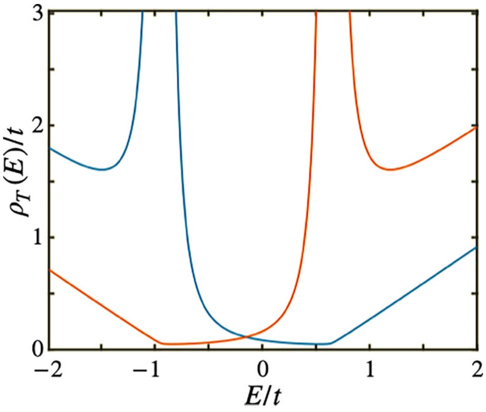

FIG. 16. Density of states at the zigzag edge of a semi-infinite TMD layer with A- (blue) and B-type (red) termination. All parameters are the same as in Fig. 2 for valley K and spin-up electrons.

For a semi-infinite zigzag layer with an A-type border, the projections of $\hat{\tau}$ into the eigenstates are

$$\hat{\tau}_{s\eta}^{++} = \hat{\tau}_{s\eta}^{--} = \frac{1}{2N_{s\eta}^2 \cos\alpha_{s\eta}}, \tag{D6a}$$

$$\hat{\tau}_{s\eta}^{+-} = \frac{\mathrm{e}^{i\alpha_{s\eta}}}{2N_{s\eta}^2 \cos\alpha_{s\eta}}, \tag{D6b}$$

$$\hat{\tau}_{s\eta}^{-+} = \frac{\mathrm{e}^{-i\alpha_{s\eta}}}{2N_{s\eta}^2 \cos\alpha_{s\eta}}, \tag{D6c}$$

which have been computed using Eq. (18). Similar expressions are obtained for border B.

The semi-infinite zigzag GF can thus be compactly written as

$$\check{G}_{a,s\eta}^{R}(x,x') = \check{g}_{s\eta}(x,x') - \mathrm{e}^{i\alpha_{s\eta}}\mathrm{e}^{ik_{s\eta}(x+x'-2x_0)}\check{M}_{s\eta}^{+-}, \tag{D7}$$

where

$$\check{M}_{s\eta}^{\epsilon\epsilon'} = \psi_{s\eta}^{\epsilon}\left(\bar{\psi}_{s\eta}^{\epsilon'}\right)^T. \tag{D8}$$

Substituting the eigenstates, Eq. (D1), we get

$$\check{G}_{a,s\eta}^{R,>}(x,x') = A\left[\frac{\mathrm{e}^{ik_{s\eta}(x-x')}}{2\cos\alpha_{s\eta}}\begin{pmatrix} N_{s\eta}^{-2} & \mathrm{e}^{-i\alpha_{s\eta}} \\ \mathrm{e}^{i\alpha_{s\eta}} & N_{s\eta}^2 \end{pmatrix} - \frac{\mathrm{e}^{i\alpha_{s\eta}}\mathrm{e}^{ik_{s\eta}(x+x'-2x_a)}}{2\cos\alpha_{s\eta}} \times \begin{pmatrix} N_{s\eta}^{-2}\mathrm{e}^{-i\alpha_{s\eta}} & -1 \\ 1 & -N_{s\eta}^2\mathrm{e}^{i\alpha_{s\eta}} \end{pmatrix}\right], \tag{D9}$$

with $A = -i/(2\hbar v_F)$.

The GF evaluated at the zigzag edge with A-atom termination reads

$$\check{G}_{a,s\eta}^{R,>}(x_a,x_a) = -\frac{i}{\hbar v_F}\begin{pmatrix} 0 & 1 \\ 0 & N_{s\eta}^2\mathrm{e}^{i\alpha_{s\eta}} \end{pmatrix}. \tag{D10}$$

Analogously, when the zigzag edge is terminated in B-type atoms, the GF adopts the same form as in Eq. (D10) with the change $N_{s\eta}^2 \to 1/N_{s\eta}^2$, cf. Eq. (48). This simple inversion plays an important role in the spectral properties of the layer, as schematically described in Fig. 7. To show this effect more clearly, we plot in Fig. 16 the density of states for each edge termination, A and B, for a semiconducting TMD, showcasing the band inversion. We note here that our continuum approach still captures the rapid atomic-scale decay of the zigzag edge states.

Finally, a compact expression for the zigzag nanoribbon GF is

$$\check{G}_{ab,s\eta}^{>}(x,x') = A\hat{D}_{s\eta}^{++}\left(\mathrm{e}^{ik_{s\eta}x}\psi_{s\eta}^{+} + \hat{r}_{s\eta}^{-+}\mathrm{e}^{-ik_{s\eta}(x-2x_b)}\psi_{s\eta}^{-}\right) \times \left(\mathrm{e}^{-ik_{s\eta}x'}\psi_{s\eta}^{+\dagger} + \hat{r}_{s\eta}^{+-}\mathrm{e}^{ik_{s\eta}(x'-2x_a)}\psi_{s\eta}^{-\dagger}\right), \tag{D11}$$

where

$$\hat{D}_{s\eta}^{++} = \left[1 - \hat{r}_{s\eta}^{+-}\hat{r}_{s\eta}^{-+}\mathrm{e}^{2ik_{s\eta}W}\right]^{-1}. \tag{D12}$$

It is thus straightforward to get the edge GF as

$$\check{G}_{ab,s\eta}^{>}(x_a,x_a) = \frac{-i}{\hbar v_F}\begin{pmatrix} 0 & \frac{1+\mathrm{e}^{2i\alpha_{s\eta}}\mathrm{e}^{i2k_{s\eta}W}}{1+\mathrm{e}^{+2i\alpha_{s\eta}}\mathrm{e}^{2ik_{s\eta}W}} \\ 0 & \frac{N_{s\eta}^2\mathrm{e}^{i\alpha_{s\eta}}\left(1-\mathrm{e}^{i2k_{s\eta}W}\right)}{1+\mathrm{e}^{+2i\alpha_{s\eta}}\mathrm{e}^{2ik_{s\eta}W}} \end{pmatrix}, \tag{D13}$$

valid when the left edge (x_a) has A-type termination. As explained above, for terminations on B atoms, Eq. (D13) is changed as $N_{s\eta}^2 \to N_{s\eta}^{-2}$.

2. Armchair Hamiltonian

Being block-diagonal, the solutions of Eq. (51) are projected into each valley, $\Psi_s = (\psi_{sK}, \psi_{sK'})^T$ with normalized eigenstates

$$\psi_{sK}^{+} = \frac{1}{\sqrt{2\cos\alpha_s}}\begin{pmatrix} N^{-1}\mathrm{e}^{-i\frac{\alpha_s}{2}} \\ N\mathrm{e}^{i\frac{\alpha_s}{2}} \end{pmatrix}, \tag{D14a}$$

$$\psi_{sK}^{-} = \frac{1}{\sqrt{2\cos\alpha_s}}\begin{pmatrix} N^{-1}\mathrm{e}^{i\frac{\alpha_s}{2}} \\ -N\mathrm{e}^{-i\frac{\alpha_s}{2}} \end{pmatrix}, \tag{D14b}$$

$$\psi_{sK'}^{+} = \frac{1}{\sqrt{2\cos\alpha_s'}}\begin{pmatrix} N'^{-1}\mathrm{e}^{i\frac{\alpha_s'}{2}} \\ -N'\mathrm{e}^{-i\frac{\alpha_s'}{2}} \end{pmatrix}, \tag{D14c}$$

$$\psi_{sK'}^{-} = \frac{1}{\sqrt{2\cos\alpha_s'}}\begin{pmatrix} N'^{-1}\mathrm{e}^{-i\frac{\alpha_s'}{2}} \\ N'\mathrm{e}^{i\frac{\alpha_s'}{2}} \end{pmatrix}, \tag{D14d}$$

and the states $\tilde{\psi}_{sn}^{\epsilon} = \hat{\sigma}_x\psi_{sn}^{\epsilon}$, $n = K, K'$, for example,

$$\tilde{\psi}_{sK'}^{-} = \frac{1}{\sqrt{2\cos\alpha_s'}}\begin{pmatrix} N'\mathrm{e}^{i\frac{\alpha_s'}{2}} \\ N'^{-1}\mathrm{e}^{-i\frac{\alpha_s'}{2}} \end{pmatrix}. \tag{D15}$$

As before, we can write $\bar{\psi}_{s\eta}^{\epsilon T} = \psi_{s\eta}^{\epsilon\dagger}$. We have defined $N \equiv N_{sK}$ and $N' \equiv N_{sK'}$, see Eq. (48), for valley K and K', respectively. Similarly, primed quantities $(\alpha_s', k_s', \dots)$ refer to valley K'. For simplicity, we omit the spin index s in the wave functions and GFs.

The semi-infinite armchair GF at the edge x_0 is

$$\check{G}_{a}^{R,<}(x_0,x_0) = \left(\Psi_K^{-} + \hat{r}_{KK}^{+-}\Psi_K^{+} + \hat{r}_{K'K}^{+-}\Psi_{K'}^{+}\right)\Psi_K^{-\dagger} + \left(\Psi_{K'}^{-} + \hat{r}_{K'K'}^{+-}\Psi_{K'}^{+} + \hat{r}_{KK'}^{+-}\Psi_{K}^{+}\right)\Psi_{K'}^{-\dagger}, \tag{D16}$$

where we have defined $\Psi_K^{\epsilon} = (\psi_K^{\epsilon}, \mathbf{0})^T$ and $\Psi_{K'}^{\epsilon} = (\mathbf{0}, \psi_{K'}^{\epsilon})^T$, with $\mathbf{0} = (0,0)^T$.

The valley-projected scalar scattering amplitudes, such as $\hat{r}_{K'K'}^{+-}$, can be recast in terms of the auxiliary scalar

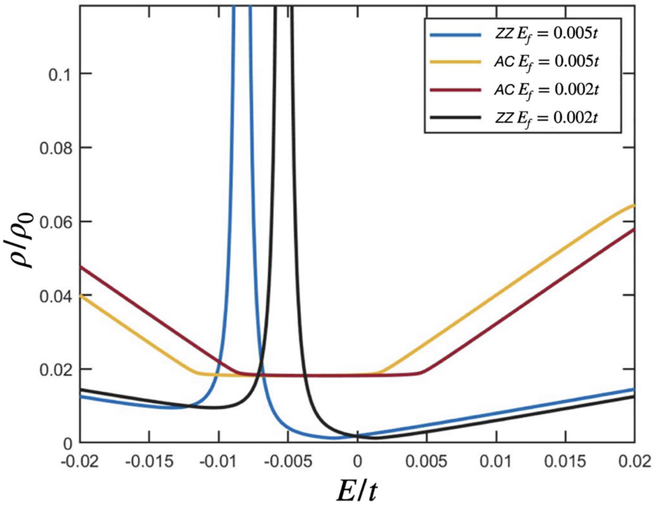

FIG. 17. Density of states at the zigzag (ZZ) and armchair (AC) edge of a semi-infinite germanene for different Fermi energies (E_f).

quantities $h_{nm}^{\epsilon\epsilon'} = \tilde{\psi}_n^{\epsilon\dagger}\psi_m^{\epsilon'}$. For instance, $\hat{r}_{K'K'}^{+-} = h_{K'K}^{++}/h_{K'K}^{-+}$. Using Eq. (D14), we get

$$h_{KK'}^{++} = \tilde{\psi}_K^{+\dagger}\psi_{K'}^{+}$$

$$= \frac{\mathrm{e}^{i\frac{(\alpha_s'-\alpha_s)}{2}}}{2\sqrt{\cos\alpha_s\cos\alpha_s'}}\left(\frac{N}{N'} - \frac{N'}{N}\mathrm{e}^{-i(\alpha_s'-\alpha_s)}\right), \tag{D17a}$$

$$h_{K'K}^{-+} = h_{KK'}^{-+} = \tilde{\psi}_K^{-\dagger}\psi_{K'}^{+}$$

$$= \frac{\mathrm{e}^{i\frac{(\alpha_s'+\alpha_s)}{2}}}{2\sqrt{\cos\alpha_s'\cos\alpha_s}}\left(\frac{N}{N'} + \frac{N'}{N}\mathrm{e}^{-i(\alpha_s'+\alpha_s)}\right), \tag{D17b}$$

$$h_{K'K}^{++} = \tilde{\psi}_{K'}^{+\dagger}\psi_{K}^{+}$$

$$= \frac{\mathrm{e}^{i\frac{(\alpha_s'-\alpha_s)}{2}}}{2\sqrt{\cos\alpha_s\cos\alpha_s'}}\left(\frac{N'}{N} - \frac{N}{N'}\mathrm{e}^{-i(\alpha_s'-\alpha_s)}\right). \tag{D17c}$$

The resulting scattering amplitudes are

$$\hat{r}_{KK}^{+-} = \mathrm{e}^{i\alpha_s}\frac{N^2\mathrm{e}^{-i\alpha_s} - N'^2\mathrm{e}^{-i\alpha_s'}}{N^2\mathrm{e}^{i\alpha_s} + N'^2\mathrm{e}^{-i\alpha_s'}}, \tag{D18a}$$

$$\hat{r}_{K'K}^{+-} = -2\frac{NN'\sqrt{\cos\alpha_s\cos\alpha_s'}}{N^2\mathrm{e}^{i\alpha_s} + N'^2\mathrm{e}^{-i\alpha_s'}}\mathrm{e}^{i\frac{\alpha_s-\alpha_s'}{2}}, \tag{D18b}$$

$$\hat{r}_{KK'}^{+-} = -2\frac{NN'\sqrt{\cos\alpha_s'\cos\alpha_s}}{N'^2\mathrm{e}^{-i\alpha_s'} + N^2\mathrm{e}^{i\alpha_s}}\mathrm{e}^{i\frac{\alpha_s-\alpha_s'}{2}}, \tag{D18c}$$

$$\hat{r}_{K'K'}^{+-} = \mathrm{e}^{i\alpha_s'}\frac{N'^2 - N^2\mathrm{e}^{-i(\alpha_s'-\alpha_s)}}{N'^2 + N^2\mathrm{e}^{i(\alpha_s'+\alpha_s)}}. \tag{D18d}$$

Finally, the armchair nanoribbon GF contains elements in all valley projections. The projection into valleys $n, m = K, K'$, $\hat{G}_{nm}^{>}(x, x')$, is shown in the main text, Eq. (58), and repeated here for completeness:

$$\hat{G}_{nm}^{>}(x, x') = \sum_{\varepsilon,\varepsilon'=\pm} f_{nm}^{\varepsilon\varepsilon'}(x, x')\hat{r}_{nm}^{>,\varepsilon\varepsilon'}\hat{M}_{nm}^{\varepsilon\varepsilon'}. \tag{D19}$$

Here, $f_{nm}^{\varepsilon\varepsilon'}(x, x') = f_n^{\varepsilon}(x)f_m^{\epsilon'}(x')$, where $f_n^{\varepsilon}(x) = \mathrm{e}^{i(K_n+\varepsilon k_n)x}$, $K_n = K, K'$, and $k_n = k_s, k_s'$. Moreover, the matrices of reflection coefficients projected into each valley subspace, $\hat{r}_{nm}^{>,\varepsilon\varepsilon'}$, with $\varepsilon, \varepsilon' = \pm$, are obtained from

$$\hat{r}_a^{+-}(x_a) = \begin{pmatrix} \frac{h_{KK'}}{h_{KK'}}\mathrm{e}^{-2ik_sx_a} & \frac{-1}{h_{K'K}}\mathrm{e}^{-i(2K+k_s+k_s')x_a} \\ \frac{-1}{h_{KK'}}\mathrm{e}^{i(2K-k_s-k_s')x_a} & \frac{h_{K'K}}{h_{K'K}}\mathrm{e}^{-2ik_s'x_a} \end{pmatrix}, \tag{D20a}$$

$$\hat{r}_b^{-+}(x_b) = \begin{pmatrix} \frac{h_{KK'}^{--}}{h_{KK'}^{+-}}\mathrm{e}^{2ik_sx_b} & \frac{-1}{h_{K'K}^{+-}}\mathrm{e}^{i(-2K+k_s+k_s')x_b} \\ \frac{-1}{h_{KK'}^{+-}}\mathrm{e}^{i(2K+k_s'+k_s)x_b} & \frac{h_{K'K}^{--}}{h_{K'K}^{+-}}\mathrm{e}^{2ik_s'x_b} \end{pmatrix}. \tag{D20b}$$

APPENDIX E: FERMI-ENERGY DEPENDENCE

The position of the Fermi level represented by E_F in Eqs. (40) and (52) becomes very important in heterostructures to represent different doping levels and electrostatic barriers. Here, we only consider isolated junctions where the effect of E_F is just a trivial shift of the band dispersion. For this reason, in the main text we set $E_F = 0$ in all plots.

For clarity, we now show the effect of a finite Fermi energy plotting in Fig. 17 the density of states at the edge of germanene semi-infinite layers with zigzag and armchair terminations. In all cases we observe how the Fermi energy shifts the position of the spectrum. The same effect takes place for germanene nanoribbons, and semi-infinite and finite TMD layers.

[1] C. Tan, X. Cao, X.-J. Wu, Q. He, J. Yang, X. Zhang, J. Chen, W. Zhao, S. Han, G.-H. Nam, M. Sindoro, and H. Zhang, Recent advances in ultrathin two-dimensional nanomaterials, Chem. Rev. (Washington, DC, U.S.) **117**, 6225 (2017).

[2] S. S. Varghese, S. H. Varghese, S. Swaminathan, K. K. Singh, and V. Mittal, Two-dimensional materials for sensing: Graphene and beyond, Electronics (Basel, Switz.) **4**, 651 (2015).

[3] C. Liu, H. Chen, S. Wang, Q. Liu, Y.-G. Jiang, D. W. Zhang, M. Liu, and P. Zhou, Two-dimensional materials for next-generation computing technologies, Nat. Nanotechnol. **15**, 545 (2020).

[4] F. Schwierz, J. Pezoldt, and R. Granzner, Two-dimensional materials and their prospects in transistor electronics, Nanoscale **7**, 8261 (2015).

[5] D. Akinwande, C. Huyghebaert, C.-H. Wang, M. I. Serna, S. Goossens, L.-J. Li, H.-S. P. Wong, and F. H. L. Koppens, Graphene and two-dimensional materials for silicon technology, Nature (London) **573**, 507 (2019).

[6] G. Fiori, F. Bonaccorso, G. Iannaccone, T. Palacios, D. Neumaier, A. Seabaugh, S. K. Banerjee, and L. Colombo, Electronics based on two-dimensional materials, Nat. Nanotechnol. **9**, 768 (2014).

[7] A. Acun, L. Zhang, P. Bampoulis, M. Farmanbar, A. van Houselt, A. N. Rudenko, M. Lingenfelder, G. Brocks,

B. Poelsema, M. I. Katsnelson, and H. J. W. Zandvliet, Germanene: The germanium analogue of graphene, J. Phys.: Condens. Matter **27**, 443002 (2015).

[8] C. Kamal and M. Ezawa, Arsenene: Two-dimensional buckled and puckered honeycomb arsenic systems, Phys. Rev. B **91**, 085423 (2015).

[9] S. Chowdhury and D. Jana, A theoretical review on electronic, magnetic and optical properties of silicene, Rep. Prog. Phys. **79**, 126501 (2016).

[10] S. Manzeli, D. Ovchinnikov, D. Pasquier, O. V. Yazyev, and A. Kis, 2D transition metal dichalcogenides, Nat. Rev. Mater. **2**, 17033 (2017).

[11] A. H. Castro Neto, F. Guinea, N. M. R. Peres, K. S. Novoselov, and A. K. Geim, The electronic properties of graphene, Rev. Mod. Phys. **81**, 109 (2009).

[12] M. Xu, T. Liang, M. Shi, and H. Chen, Graphene-like two-dimensional materials, Chem. Rev. (Washington, DC, U.S.) **113**, 3766 (2013).

[13] J. Wang, S. Deng, Z. Liu, and Z. Liu, The rare two-dimensional materials with Dirac cones, Natl. Sci. Rev. **2**, 22 (2015).

[14] D. Jariwala, V. K. Sangwan, L. J. Lauhon, T. J. Marks, and M. C. Hersam, Emerging device applications for semiconducting two-dimensional transition metal dichalcogenides, ACS Nano **8**, 1102 (2014).

[15] J. R. Schaibley, H. Yu, G. Clark, P. Rivera, J. S. Ross, K. L. Seyler, W. Yao, and X. Xu, Valleytronics in 2D materials, Nat. Rev. Mater. **1**, 16055 (2016).

[16] Y. P. Feng, L. Shen, M. Yang, A. Wang, M. Zeng, Q. Wu, S. Chintalapati, and C.-R. Chang, Prospects of spintronics based on 2D materials, Wiley Interdiscip. Rev. Comput. Mol. Sci. **7**, e1313 (2017).

[17] C. Zhu, D. Du, and Y. Lin, Graphene-like 2D nanomaterial-based biointerfaces for biosensing applications, Biosens. Bioelectron. **89**, 43 (2017).

[18] E. C. Ahn, 2D materials for spintronic devices, npj 2D Mater. Appl. **4**, 17 (2020).

[19] T. O. Wehling, A. M. Black-Schaffer, and A. V. Balatsky, Dirac materials, Adv. Phys. **63**, 1 (2014).

[20] J. Cayssol, Introduction to Dirac materials and topological insulators, C. R. Phys. **14**, 760 (2013).

[21] M. König, S. Wiedmann, C. Brüne, A. Roth, H. Buhmann, L. W. Molenkamp, X.-L. Qi, and S.-C. Zhang, Quantum spin Hall insulator state in HgTe quantum wells, Science **318**, 766 (2007).

[22] I. Knez, R.-R. Du, and G. Sullivan, Evidence for helical edge modes in inverted InAs/GaSb quantum wells, Phys. Rev. Lett. **107**, 136603 (2011).

[23] M. Z. Hasan and C. L. Kane, Colloquium: Topological insulators, Rev. Mod. Phys. **82**, 3045 (2010).

[24] L. Kou, Y. Ma, Z. Sun, T. Heine, and C. Chen, Two-dimensional topological insulators: Progress and prospects, J. Phys. Chem. Lett. **8**, 1905 (2017).

[25] Y. Xia, D. Qian, D. Hsieh, L. Wray, A. Pal, H. Lin, A. Bansil, D. Grauer, Y. S. Hor, R. J. Cava, and M. Z. Hasan, Observation of a large-gap topological-insulator class with a single Dirac cone on the surface, Nat. Phys. **5**, 398 (2009).

[26] D. Hsieh, D. Qian, L. Wray, Y. Xia, Y. S. Hor, R. J. Cava, and M. Z. Hasan, A topological Dirac insulator in a quantum spin Hall phase, Nature (London) **452**, 970 (2008).

[27] Y. L. Chen, J. G. Analytis, J.-H. Chu, Z. K. Liu, S.-K. Mo, X. L. Qi, H. J. Zhang, D. H. Lu, X. Dai, Z. Fang, S. C. Zhang, I. R. Fisher, Z. Hussain, and Z.-X. Shen, Experimental realization of a three-dimensional topological insulator, $\mathrm{Bi_2Te_3}$, Science **325**, 178 (2009).

[28] J. Kruthoff, J. de Boer, J. van Wezel, C. L. Kane, and R.-J. Slager, Topological classification of crystalline insulators through band structure combinatorics, Phys. Rev. X **7**, 041069 (2017).

[29] B. Bradlyn, L. Elcoro, J. Cano, M. G. Vergniory, Z. Wang, C. Felser, M. I. Aroyo, and B. A. Bernevig, Topological quantum chemistry, Nature (London) **547**, 298 (2017).

[30] C. C. Liu, W. Feng, and Y. Yao, Quantum spin Hall effect in silicene and two-dimensional germanium, Phys. Rev. Lett. **107**, 076802 (2011).

[31] M. Ezawa, A topological insulator and helical zero mode in silicene under an inhomogeneous electric field, New J. Phys. **14**, 033003 (2012).

[32] M. Ezawa, Valley-polarized metals and quantum anomalous Hall effect in silicene, Phys. Rev. Lett. **109**, 055502 (2012).

[33] C. H. Lewenkopf and E. R. Mucciolo, The recursive Green's function method for graphene, J. Comput. Electron. **12**, 203 (2013).

[34] G. Thorgilsson, G. Viktorsson, and S. I. Erlingsson, Recursive Green's function method for multi-terminal nanostructures, J. Comput. Phys. **261**, 256 (2014).

[35] M. Ezawa, Monolayer topological insulators: Silicene, germanene, and stanene, J. Phys. Soc. Jpn. **84**, 121003 (2015).

[36] S. Gerivani and H. Milani Moghaddam, Intrinsic half-metallic properties of MnHm (M: Fe, V, Co, and Cr) in various space groups: A first-principles study, J. Magn. Magn. Mater. **547**, 168758 (2022).

[37] J. M. Marmolejo-Tejada and J. Velasco-Medina, Review on graphene nanoribbon devices for logic applications, Microelectron. J. **48**, 18 (2016).

[38] H. Wang, H. S. Wang, C. Ma, L. Chen, C. Jiang, C. Chen, X. Xie, A.-P. Li, and X. Wang, Graphene nanoribbons for quantum electronics, Nat. Rev. Phys. **3**, 791 (2021).

[39] L. Brey and H. A. Fertig, Electronic states of graphene nanoribbons studied with the Dirac equation, Phys. Rev. B **73**, 235411 (2006).

[40] J. Wurm, K. Richter, and İ. Adagideli, Edge effects in graphene nanostructures: From multiple reflection expansion to density of states, Phys. Rev. B **84**, 075468 (2011).

[41] M. Aidelsburger, S. Nascimbene, and N. Goldman, Artificial gauge fields in materials and engineered systems, C. R. Phys. **19**, 394 (2018).

[42] D. A. Manjarrés, W. J. Herrera, and S. Gómez, Andreev levels in a graphene–superconductor surface, Phys. B (Amsterdam, Neth.) **404**, 2799 (2009).

[43] W. J. Herrera, P. Burset, and A. L. Yeyati, A Green function approach to graphene–superconductor junctions with well-defined edges, J. Phys.: Condens. Matter **22**, 275304 (2010).

[44] P. Burset, W. Herrera, and A. Levy Yeyati, Proximity-induced interface bound states in superconductor-graphene junctions, Phys. Rev. B **80**, 041402(R) (2009).

[45] G. Tkachov, Dirac fermion quantization on graphene edges: Isospin-orbit coupling, zero modes, and spontaneous valley polarization, Phys. Rev. B **79**, 045429 (2009).

[46] G. Tkachov and M. Hentschel, Coupling between chirality and pseudospin of Dirac fermions: Non-analytical particle-hole

asymmetry and a proposal for a tunneling device, Phys. Rev. B **79**, 195422 (2009).

[47] J.-W. Rhim, J. H. Bardarson, and R.-J. Slager, Unified bulk-boundary correspondence for band insulators, Phys. Rev. B **97**, 115143 (2018).

[48] S. Gómez Páez, C. Martínez, W. J. Herrera, A. Levy Yeyati, and P. Burset, Dirac point formation revealed by Andreev tunneling in superlattice-graphene/superconductor junctions, Phys. Rev. B **100**, 205429 (2019).

[49] O. E. Casas, S. G. Páez, and W. J. Herrera, A Green's function approach to topological insulator junctions with magnetic and superconducting regions, J. Phys.: Condens. Matter **32**, 485302 (2020).

[50] T. L. van den Berg, A. De Martino, M. R. Calvo, and D. Bercioux, Volkov-Pankratov states in topological graphene nanoribbons, Phys. Rev. Res. **2**, 023373 (2020).

[51] M. Andelkovic, Kh. Yu. Rakhimov, A. Chaves, G. R. Berdiyorov, and M. V. Milošević, Wave-packet propagation in a graphene geometric diode, Phys. E (Amsterdam, Neth.) **147**, 115607 (2023).

[52] F. J. A. Linard, V. N. Moura, L. Covaci, M. V. Milošević, and A. Chaves, Wave-packet scattering at a normal-superconductor interface in two-dimensional materials: A generalized theoretical approach, Phys. Rev. B **107**, 165306 (2023).

[53] B. Lu and Y. Tanaka, Study on Green's function on topological insulator surface, Philos. Trans. R. Soc., A **376**, 20150246 (2018).

[54] P. Burset, A. Levy Yeyati, and A. Martín-Rodero, Microscopic theory of the proximity effect in superconductor-graphene nanostructures, Phys. Rev. B **77**, 205425 (2008).

[55] T. Ando, Theory of electronic states and transport in carbon nanotubes, J. Phys. Soc. Jpn. **74**, 777 (2005).

[56] A. Kormányos, G. Burkard, M. Gmitra, J. Fabian, V. Zólyomi, N. D. Drummond, and V. Fal'ko, $\mathbf{k}\cdot\mathbf{p}$ theory for two-dimensional transition metal dichalcogenide semiconductors, 2D Mater. **2**, 022001 (2015).

[57] X. Qian, J. Liu, L. Fu, and J. Li, Quantum spin Hall effect in two-dimensional transition metal dichalcogenides, Science **346**, 1344 (2014).

[58] D. Xiao, G.-B. Liu, W. Feng, X. Xu, and W. Yao, Coupled spin and valley physics in monolayers of MoS_2 and other group-VI dichalcogenides, Phys. Rev. Lett. **108**, 196802 (2012).

[59] L. Brey and H. A. Fertig, Edge states and the quantized Hall effect in graphene, Phys. Rev. B **73**, 195408 (2006).

[60] S. Fang, R. Kuate Defo, S. N. Shirodkar, S. Lieu, G. A. Tritsaris, and E. Kaxiras, Ab initio tight-binding Hamiltonian for transition metal dichalcogenides, Phys. Rev. B **92**, 205108 (2015).

[61] L. Ma, J. Wang, and F. Ding, Recent progress and challenges in graphene nanoribbon synthesis, ChemPhysChem **14**, 47 (2013).

[62] C. Si, J. Liu, Y. Xu, J. Wu, B.-L. Gu, and W. Duan, Functionalized germanene as a prototype of large-gap two-dimensional topological insulators, Phys. Rev. B **89**, 115429 (2014).

[63] A. Molle, J. Goldberger, M. Houssa, Y. Xu, S.-C. Zhang, and D. Akinwande, Buckled two-dimensional Xene sheets, Nat. Mater. **16**, 163 (2017).

[64] G. M. Rutter, J. N. Crain, N. P. Guisinger, T. Li, P. N. First, and J. A. Stroscio, Scattering and interference in epitaxial graphene, Science **317**, 219 (2007).

[65] L. Rosales and J. W. González, Transport properties of two finite armchair graphene nanoribbons, Nanoscale Res. Lett. **8**, 1 (2013).

[66] C. L. Kane and E. J. Mele, Quantum spin Hall effect in graphene, Phys. Rev. Lett. **95**, 226801 (2005).

[67] P. Bampoulis, C. Castenmiller, D. J. Klaassen, J. van Mil, Y. Liu, C.-C. Liu, Y. Yao, M. Ezawa, A. N. Rudenko, and H. J. W. Zandvliet, Quantum spin hall states and topological phase transition in germanene, Phys. Rev. Lett. **130**, 196401 (2023).

[68] A. Raja, A. Chaves, J. Yu, G. Arefe, H. M. Hill, A. F. Rigosi, T. C. Berkelbach, P. Nagler, C. Schüller, T. Korn, C. Nuckolls, J. Hone, L. E. Brus, T. F. Heinz, D. R. Reichman, and A. Chernikov, Coulomb engineering of the bandgap and excitons in two-dimensional materials, Nat. Commun. **8**, 15251 (2017).

[69] A. Chaves, J. G. Azadani, H. Alsalman, D. R. da Costa, R. Frisenda, A. J. Chaves, S. H. Song, Y. D. Kim, D. He, J. Zhou, A. Castellanos-Gomez, F. M. Peeters, Z. Liu, C. L. Hinkle, S.-H. Oh, P. D. Ye, S. J. Koester, Y. H. Lee, P. Avouris, X. Wang, and T. Low, Bandgap engineering of two-dimensional semiconductor materials, npj 2D Mater. Appl. **4**, 29 (2020).

[70] L. Tao, E. Cinquanta, D. Chiappe, C. Grazianetti, M. Fanciulli, M. Dubey, A. Molle, and D. Akinwande, Silicene field-effect transistors operating at room temperature, Nat. Nanotechnol. **10**, 227 (2015).

[71] T. Roy, M. Tosun, J. S. Kang, A. B. Sachid, S. B. Desai, M. Hettick, C. C. Hu, and A. Javey, Field-effect transistors built from all two-dimensional material components, ACS Nano **8**, 6259 (2014).

[72] M. H. D. Guimarães, H. Gao, Y. Han, K. Kang, S. Xie, C.-J. Kim, D. A. Muller, D. C. Ralph, and J. Park, Atomically thin ohmic edge contacts between two-dimensional materials, ACS Nano **10**, 6392 (2016).

[73] F. Léonard and A. A. Talin, Electrical contacts to one- and two-dimensional nanomaterials, Nat. Nanotechnol. **6**, 773 (2011).

[74] A. Allain, J. Kang, K. Banerjee, and A. Kis, Electrical contacts to two-dimensional semiconductors, Nat. Mater. **14**, 1195 (2015).

[75] L. Wang, I. Meric, P. Y. Huang, Q. Gao, Y. Gao, H. Tran, T. Taniguchi, K. Watanabe, L. M. Campos, D. A. Muller, J. Guo, P. Kim, J. Hone, K. L. Shepard, and C. R. Dean, One-dimensional electrical contact to a two-dimensional material, Science **342**, 614 (2013).

[76] M. V. Milošević and D. Mandrus, 2D Quantum materials: Magnetism and superconductivity, J. Appl. Phys. **130**, 180401 (2021).

[77] W.-T. Lu and Q.-F. Sun, Electrical control of crossed Andreev reflection and spin-valley switch in antiferromagnet/superconductor junctions, Phys. Rev. B **104**, 045418 (2021).

[78] M. Shafiei, F. Fazileh, F. M. Peeters, and M. V. Milošević, Controlling the hybridization gap and transport in a thin-film topological insulator: Effect of strain, and electric and magnetic field, Phys. Rev. B **106**, 035119 (2022).

[79] N. Kheirabadi and A. Langari, Quantum nonlinear planar Hall effect in bilayer graphene: An orbital effect of a steady in-plane magnetic field, Phys. Rev. B **106**, 245143 (2022).